

LUNDS TEKNISKA HÖGSKOLA
MASTER'S THESIS

Initial Characterizations of a Pixelated
Thermal-Neutron Detector

Author:
Amanda Jalgén

Supervisor:
Kevin Fissum
Co-Supervisor:
Hanno Perrey

*A thesis submitted in fulfillment of the requirements
for the degree of Master of Science
in the*

Department of Physics
Division of Nuclear Physics



LUND
UNIVERSITY

Abstract

The purpose of this project was to develop a better understanding of the response of a pixelated thermal-neutron detector, which will be used as a thermal-neutron detector at one of the beam lines at the European Spallation Source in Lund, Sweden. The detector consists of a thin Lithium6-glass scintillator, a multi-anode photomultiplier tube and associated read-out electronics. Initial characterizations of the response to laser light and a collimated alpha-particle beam were performed in collaboration with the Department of Nuclear Physics at the University of Glasgow. The response of the prototype to the laser light was demonstrated to be reproducible. The absolute gain for each pixel provided by the manufacturer for the multi-anode photomultiplier tube was not reproducible. For the first time ever, the response of the prototype to a collimated alpha-particle beam was determined. Pixel-to-pixel gain variations were gain corrected using both the measured laser correction matrix and the data sheet from the manufacturer. Qualitative similarities between the results using the two calibration methods clearly exist. Further study is warranted.

Acknowledgements

Throughout this thesis, I have been helped many people. I would like to start by thanking Seian Al Jebali and the rest of the people at the University of Glasgow for all their assistance during our trip there. I would also like to thank the ESS Detector Group for all their encouragement and support. Finally, I would like to express my deepest gratitude to everyone in the Source-based Neutron Irradiation Group (SoNnIG) at the Department of Nuclear Physics, Lund University. I would also want to give a special thanks to Kevin Fissum and Hanno Perrey, the supervisor and co-supervisor of this thesis.

Contents

Abstract	i
Acknowledgements	iii
Contents	vi
List of Figures	viii
List of Tables	ix
Abbreviations	x
1 Introduction	1
1.1 Overview	1
1.2 The neutron	1
1.3 Spallation	3
1.4 Moderation	4
1.5 Beam guides	5
1.6 Small-Angle Neutron Scattering	5
1.6.1 Small-K Advanced Diffractometer	6
1.6.2 Solid-State Neutron Detector	7
1.7 Project motivation	8
2 Materials and methods	9
2.1 Scintillators	9
2.1.1 Glass scintillators	9
2.1.2 Lithium6-glass	10
2.2 Photomultiplier tubes	11
2.2.1 Single anode	11
2.2.2 Multi anode	12
2.3 Basic electronic concepts	14
2.3.1 Threshold	14
2.3.2 Walk effect and constant-fraction discriminator	14
2.3.3 Time-to-digital converter	15
2.3.4 Charge-to-digital converter	15
2.4 Hamamatsu calibration data sheet	17
2.4.1 Pedestal correction and fitting	18
2.5 Measurements	22
2.5.1 Test bench at the University of Glasgow	22

2.5.2	Laser irradiations	23
2.5.3	Alpha-particle irradiations	25
3	Results and discussion	29
3.1	Calibration gain maps	29
3.1.1	Reproducibility test	29
3.1.2	Hamamatsu vs. laser calibration	31
3.2	Alpha-particle irradiation response	36
4	Summary and outlook	41
4.1	Summary	41
4.2	Suggestions for improvements	42
4.3	Future outlook	42
A	Contribution of the author	45
B	Self reflection	47
C	Construction of a light-tight optical box	49
C.1	Construction	49
C.2	Light-tightness verification of the box	51
C.2.1	First pre-measurement	51
C.2.2	Second pre-measurement	52
C.2.3	Measurement of light leakage	52
C.3	Conclusion	53
	References	55

List of Figures

1.1	Proton and neutron quark structure	2
1.2	The process of spallation	3
1.3	Neutron reflection or transmission depending on critical angle . .	5
1.4	Small-angle neutron scattering	6
1.5	Overview of SKADI	6
1.6	Illustration of SoNDe modules	7
2.1	Electronic-band structure of a glass scintillator	10
2.2	Scintillator coupled to a PMT	11
2.3	Photograph of a MaPMT	12
2.4	Signal multiplication within a MaPMT	13
2.5	QDC discriminator settings and the walk effect	14
2.6	Constant-fraction discriminator principle	15
2.7	QDC spectrum	15
2.8	QDC concept	16
2.9	QDC pedestal concept	16
2.10	Hamamatsu test setup	18
2.11	QDC spectra	19
2.12	Pedestal correction and Gaussian-fitting procedures	20
2.13	Gaussian gain-fitting procedure	21
2.14	Test-bench setup at the University of Glasgow University	22
2.15	Setup used for reading out the dynode 12 signal.	23
2.16	Setup for laser measurements	24
2.17	Americium241 decay to Neptunium237	25
2.18	Range of alpha particles in Lithium6-glass	26
2.19	Setup for alpha-particle measurements	27
3.1	Normalized reproducibility test	29
3.2	Laser gain map for pixel 29/QDC 38	30
3.3	Spectra for pixel 29/QDC 38, 37/40 and 45/42	31
3.4	Visualization of the gain maps for both calibrations	33
3.5	Gain differences	35
3.6	Corrected alpha-particle gain maps.	37
3.7	Illustration of misaligned MaPMT	38

3.8	Alpha-particle gain corresponding to pixel 29/QDC38.	39
C.1	First step towards constructing the optical box	49
C.2	First version of the patch panel	50
C.3	Second version of the patch panel	50
C.4	Setup inside the optical box	51
C.5	Setup with the box closed	51

List of Tables

1.1	Neutron-energy ranges	3
2.1	Specifications for GS20 Lithium6-glass	11
2.2	Specifications for the Hamamatsu MaPMT H8500C	13
2.3	Relative gain for each pixel/QDC from Hamamatsu data sheet	17
3.1	Gains obtained from data-sheet and laser calibration	32
3.2	Mean gain values for each pixel for alpha-particle irradiation	36
A.1	Summary of the contribution of the author to this project	45
C.1	Results from the final leakage measurement	53

Abbreviations

CCD	C harge- C oupled D evice
CFD	C onstant- F raction D iscriminator
ESS	E uropean S pallation S ource
LINAC	L INear A Ccelerator
MaPMT	M ulti-anode P hoto- M ultiplier T ube
NDF	N eutral D ensity F ilter
NIM	N uclear I nstrumentation M odule
PMT	P hoto- M ultiplier T ube
QDC	C harge(Q)-to- D igital C onverter
SANS	S mall- A ngle N eutron S cattering
SKADI	S mall- K A dvanced D iffractometer
SoNDe	S olid- S tate N eutron D etector
TDC	T ime-to- D igital C onverter
TTL	T ransistor- T ransistor L ogic

Chapter 1

Introduction

1.1 Overview

In Lund, Sweden, the European Spallation Source (ESS) is currently being built and will be finished in 2023. At ESS, protons will be accelerated and then collide with a target consisting of a rotating wheel of tungsten [1]. The protons will be accelerated to almost the speed of light using a 602 m linear accelerator (LINAC). During the collisions, free neutrons will be produced. These neutrons will then be moderated and guided along the neutron beam guides towards instrument stations, where scientists can use them for their research.

One of many challenges will be the development of detectors used for the different instrument stations. This report will detail a small part of that challenge; more specifically, the development of the Solid-State Neutron Detector (SoNDe). This detector will consist of Lithium6-glass as a thermal-neutron sensitive scintillator, multi-anode photomultiplier tubes (MaPMTs) and read-out electronics. When a neutron interacts with the Lithium6-glass, an alpha particle and a triton will be produced. Since the neutron itself has no charge, the detection is instead based on detecting these particles. In this work, the response of a SoNDe-module prototype to alpha irradiation will be studied to facilitate a better understanding of the behavior of the detector and how it will function under neutron irradiation.

1.2 The neutron

The neutron was discovered in 1932 by James Chadwick who was awarded the Nobel prize in physics in 1935 for this discovery [2]. Neutrons, together with protons and electrons, are what makes up the atom and matter as we know it. Neutrons are responsible for the existence of nuclei. This is because there would not be any nuclei if they only consisted of protons as protons have equal electric charge and would overwhelmingly repel each other. For almost thirty years,

physicists thought that these nucleons were fundamental but it was later proven that both protons and neutrons consist of quarks. Quarks are now thought to be fundamental.

The proton consists of two “up” quarks and one “down” quark while the neutron consists of one “up” quark and two “down” quarks, see Fig. 1.1. These quarks are held together by the strong force, an attractive force for nucleons within a distance of 1 fm from each other.

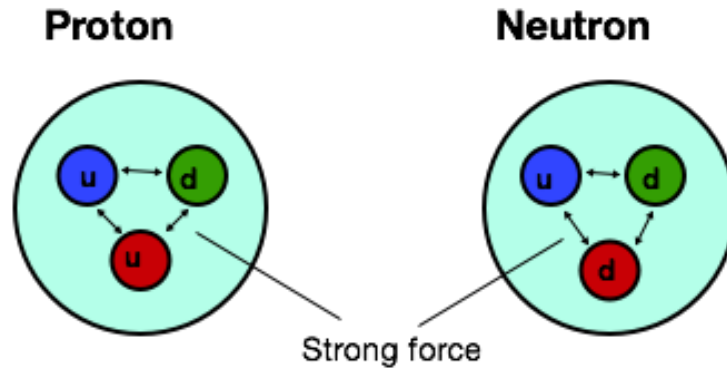


Figure 1.1: Proton and neutron quark structure. An up quark is represented with “u” and a down quark with “d”.

The balance between this strong force and the Coulomb force, which is a repulsive force between the protons over an infinite distance, determines if a collection of nucleons may form a stable nucleus or not. Neutrons may thus be thought of as the “glue” which holds together the atomic nucleus. Different combinations of protons and neutrons are called isotopes. Some isotopes are stable and do not decay into other elements while other isotopes are unstable and will decay into other elements. During the decay process, radiation is released.

Since the neutron has no electric charge, it cannot interact with electrons in matter by the Coulomb interaction. Atomic electrons are thus essentially invisible to neutrons. The charge of protons in atomic nuclei does not hinder neutrons either. They can therefore penetrate material largely without interference and because of this capability, can be used advantageously for imaging and material science.

The probability for the type of neutron matter interaction that may occur is strongly dependent on the energy of the neutron. Neutrons are thus typically grouped with regard to energy, see Table 1.1.

Table 1.1: Neutron-energy ranges. Thermal neutrons are in thermal equilibrium with their surroundings.

Type	Energy (eV)
Cold	0 – 0.025
Thermal	0.025
Epithermal	~ 1
Fast	$> 1 \cdot 10^6$

Generally speaking, the main interaction mechanism for cold and thermal neutrons is absorption while for fast neutrons, it is scattering.

1.3 Spallation

Bound neutrons are stable but free neutrons are unstable and have a mean lifetime of about 15 minutes before they decay via β^- -emission to a stable proton [3]. Neutrons can be freed using a variety of methods. The methods can range from naturally (such as radioactive sources and cosmic-rays interacting in the upper atmosphere) to man-made (such as nuclear reactors and spallation). Spallation is a process where high-energy charged particles collide with a heavy metal target. A model commonly used to explain this is the “break” in billiards. Here, during the first shot of the game, the white cue ball hits and breaks apart the stable triangle of colored balls, giving each of them energy to travel in different directions. In the spallation model, the cue ball represents the incoming high-energy proton and the stable triangle of colored balls is the spallation target. Some of the out-coming colored balls are neutrons freed from the target after the collision, see Fig. 1.2.

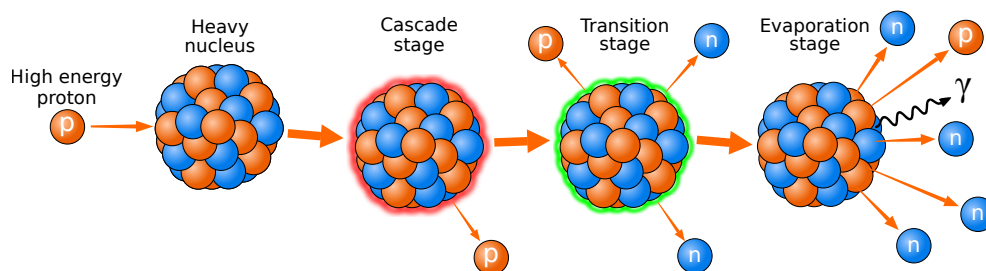


Figure 1.2: The process of spallation. A high-energy proton (red) collides with a heavy nucleus. The nucleus then passes through three stages: the Cascade stage (red outline), the Transition stage (green outline) and the Evaporation stage (rightmost image). This results in neutrons (blue) and other forms of radiation.

The evaporation stage results in the most free neutrons. Figure from [4].

The process of freeing neutrons occurs in three main stages: Cascade, Transition

and Evaporation [5]. The Cascade stage is when the energetic incoming proton strikes the target and transfers energy to the individual nucleons which might result in the release of high-energy particles capable of further spallation. In the Transition stage, the energy transferred to the individual nucleons spreads through the nucleus, resulting in several nucleons possibly being ejected and the nucleus ending up in a highly excited state. The subsequent de-excitation of the nucleus happens in the Evaporation stage and several free neutrons, protons and other forms of radiation may be emitted. Studies have shown that the number of neutrons released is proportional to the atomic number of the target material [6], but other factors such as thermal conductivity and thermal expansion also play a role. Popular materials for spallation targets are mercury, lead, tungsten and tantalum since they are neutron rich and relatively easy to handle.

1.4 Moderation

The emitted energy of the proton beam in the spallation process is extremely high and the neutrons are therefore also highly energetic. For the neutrons to be useful for the users at ESS, they have to be slowed down, or “moderated”. This is because high-energy neutrons are very deeply penetrating and will simply pass through most samples, since there is little with which they can interact.

For the applications at ESS, cold neutrons and thermal neutrons are of most interest. At these energies, the wavelength of the neutrons is on the same order of magnitude as the inter-atomic distance (10^{-10} m). The relation between wavelength and momentum of the neutron (and thus energy) is given by de Broglie wavelength [7]

$$\lambda = \frac{h}{p_n} = \frac{h}{\sqrt{2 \cdot m_n \cdot E_{kin}}} \approx 10^{-10} \text{ m},$$

where λ is the wavelength, p_n is the momentum and h is the Planck constant. Having the same wavelength as the interatomic distance allows for the investigation of atomic phenomenon and makes neutrons with this energy excellent atomic probes.

Moderation is a process where neutrons interact with a moderator material through scattering and lose some of their energy. Moderator material is often rich in hydrogen or some other light nuclei. The moderating process will in general continue until the neutrons reach thermal equilibrium with the surroundings. At this point, the neutron will most likely be absorbed by the moderator. Since the goal is only to slow down the neutrons, the choice of the size and composition of the moderator material is important to produce the maximum number of neutrons with the correct energy for the study at hand.

1.5 Beam guides

After the neutrons have been moderated to the desired energy, they must be transported to the instrument stations and focused on the sample. This is done using beam guides. For charged particles, an external magnetic field is often used to transport and focus. But since the neutron has no charge, its wavelike characteristics must instead be used to create a neutron “mirror” or “waveguide” to guide the neutrons. For the neutrons to be reflected at the surface of the wave guide and not absorbed, the incident angle of the neutron has to be smaller than the critical angle, see Fig. 1.3. The critical angle is a material characteristic which depends on the index of refraction and the atomic mass of the coating material of the beam guide in combination with the energy of the neutron.

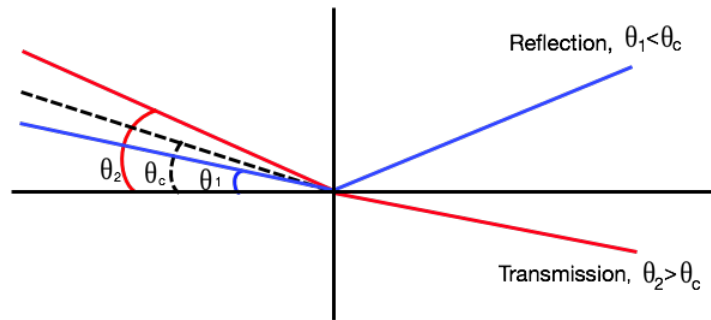


Figure 1.3: Neutron reflection or transmission depending on critical angle. Two different angles of incidence, θ_1 (blue) and θ_2 (red), and the critical angle, θ_c are shown. Neutrons striking the beam-guide surface with the angle θ_1 will be reflected while those striking the surface with the angle θ_2 will be transmitted and lost.

1.6 Small-Angle Neutron Scattering

Small-angle neutron scattering (SANS) is a technique where the neutron beam incident upon the sample elastically scatters via nuclear interactions with the sample nuclei. The degree of deflection from the original trajectory is only marginal, hence the name “small angle”. The detector counts the number of neutrons scattered as a function of angle and energy, see Fig. 1.4. It is then possible to determine the size, arrangement and interaction of the components in the sample.

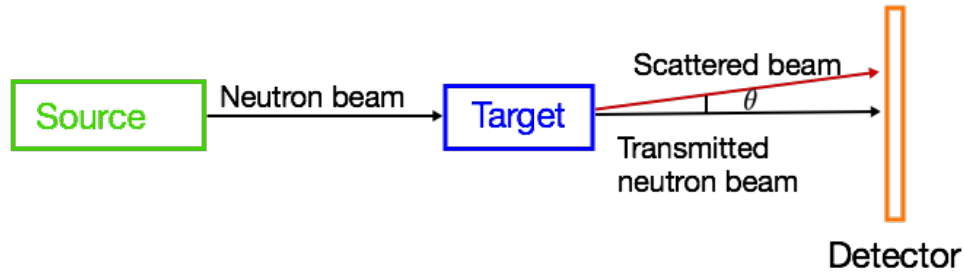


Figure 1.4: Small-angle neutron scattering. A neutron beam incident upon the target is scattered through a small angle and detected in a detector.

1.6.1 Small-K Advanced Diffractometer

One of the early instruments at ESS will be the Small-K Advanced Diffractometer (SKADI) [8], which is a SANS instrument. The SKADI project is a German, French, and Dutch collaboration. An overview of the instrument can be seen in Fig. 1.5, recall also Fig. 1.4.

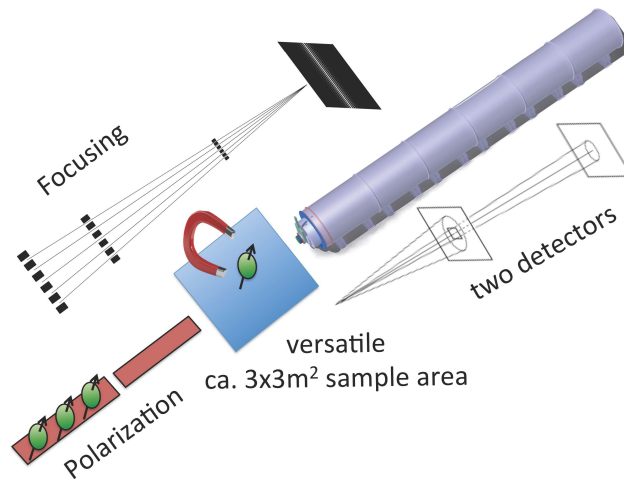


Figure 1.5: Overview of SKADI. Neutrons are incident on samples from the left and may be detected in one of the two detector planes which provide a large angular coverage [9].

The instrument consists from left to right in Fig. 1.5 of the neutron beam, a sample area and two detector planes. The total length of the instrument is 60 m, where the detector accounts for 20 m.

1.6.2 Solid-State Neutron Detector

The detector to be used to instrument SKADI is the Solid-state Neutron Detector (SoNDe) [8]. Since ESS will provide a neutron beam with much higher flux than existing facilities [10] in the depth of a Helium3 crisis [11], a new kind of detector has to be developed. The project of developing SoNDe is being coordinated by Jülich Centre for Neutron Science (JCNS) [12]. Other members of the project are Laboratoire Léon-Brillouin (LLB) [13] in France, ESS and Lund University in Lund, Sweden and the Norwegian company Integrated Detector Electronics AS (IDEAS) [14].

For this project, the H8500C MaPMT from the Japanese company Hamamatsu will be used. A schematic of the detector can be seen in Fig. 1.6. More details about the MaPMT are presented in Sec. 2.2.2.

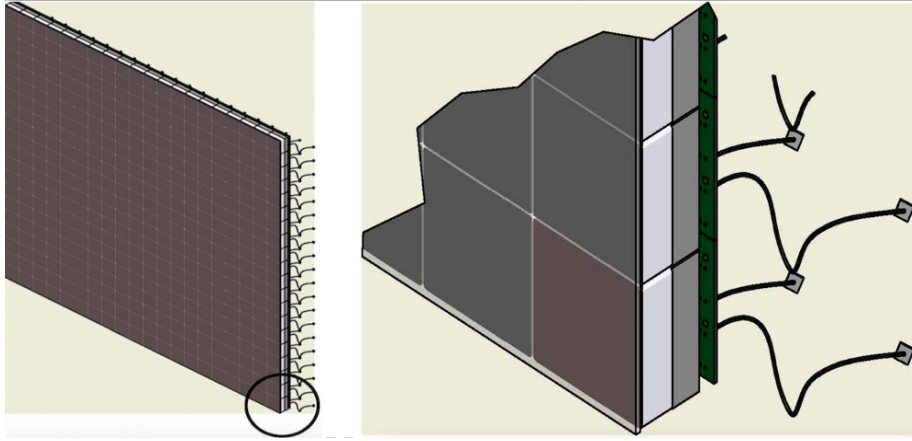


Figure 1.6: Illustration of SoNDe modules. Left panel: The entire detector with $20 \times 20 = 400$ units. Right panel: The bottom right corner focusing on a single SoNDe module. Each SoNDe module will consist of a scintillator, a MaPMT and the necessary read-out electronics [9].

Each SoNDe module will consist of a Lithium6-glass scintillator, MaPMT and read-out electronics. Photomultiplier tube (PMT) technology is well-established but conventional PMTs have a diameter of around 10 cm. For the SoNDe detector, with the help of MaPMTs, this critical parameter may be reduced to around 5 mm. Having “smaller” PMTs makes it possible to have more in the same area, which greatly improves the position resolution and the corresponding attainable count rate.

1.7 Project motivation

The focus of this thesis is to develop a better understanding of the response of a SoNDe-module prototype by performing initial characterizations of the response with laser light and a collimated alpha-particle beam.

First, the data sheet describing the MaPMT itself provided by the manufacturer will be investigated using the Laser-Mapping Facility at the University of Glasgow. Then, for the first time ever, an entire SoNDe-module prototype consisting of MaPMT and Lithium6-glass scintillator will be systematically irradiated with a well-defined alpha-particle beam to study the position dependence of the response. And finally, a project summary is offered together with ideas for moving forward with the project. A new series of investigations which will further improve the understanding of the device is suggested.

Chapter 2

Materials and methods

2.1 Scintillators

A scintillator is a detector material which converts ionizing radiation to visible light. The electrons from the atoms in the scintillator material are excited by the incoming radiation and “jump” to a higher state. Later, when they de-excite, the excess energy is sent out as a flash of light, also called a scintillation. The amount of scintillation light is often directly proportional to the energy deposited by the incident particle. The scintillator detector is generally a fast detector since the rise and fall times of the pulses are relatively short compared to other detector types. The fast time response leads to the detector having a better time resolution since it can separate pulses which arrive closer in time. There are many kinds of scintillators, all with unique properties, which makes different scintillators suitable for detection of different radiations, including neutrons.

2.1.1 Glass scintillators

Glasses are amorphous materials, which lack the long-range order which crystals have. The production of scintillation light is dependent upon their electronic band structure [15]. This is due to the fact that glasses possess band gaps because of regularities in their atomic structure. The scintillation process within a glass scintillator can be seen in Fig. 2.1.

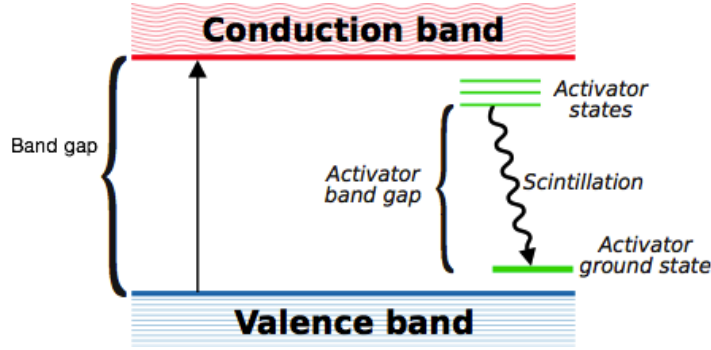


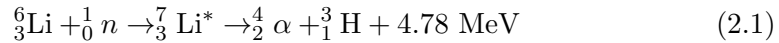
Figure 2.1: Electronic-band structure of a glass scintillator. An electron is excited from the valence band (blue) to the conduction band (red). The de-excitation, via the near-lying activator states (green), to the activator ground state results in scintillation light.

An incoming charged particle or photon excites an electron from the valence band to the conduction band. The electron de-excites back to the valence band, emitting a photon in the process. This process does not generate visible scintillation light. Activators are often added to the glass, resulting in energy states within the band gap that enable lower-energy transitions. One of several reasons for adding these activators is that typical light detectors (e.g. PMTs) are most sensitive to wavelengths in the lower end of the visible spectrum (in particular, blue) [16]. By adding the activator states, the wavelength of the scintillation light may be tuned to match the PMT.

One type of glass scintillator is Cerium-activated Lithium-glass [17]. It has a relatively low scintillation-light output compared to other kinds of scintillator. The decay time for glass scintillators is around a few 10s of ns. Cerium-activated Lithium-glass is mostly used for neutron detection but is sensitive to beta and gamma radiation as well.

2.1.2 Lithium6-glass

One specific type of Lithium-glass scintillator is enriched Lithium6-glass, GS20. When a thermal neutron interacts with the Lithium6-glass, absorption occurs [18], see Eq. 2.1.



The energies for the product particles are 2.04 MeV for the alpha particle and 2.72 MeV for the triton [19]. These charged particles will then interact with the glass. This will result in that the outermost electron of cerium(III)(Ce^{3+}), which the glass is doped with, will enter an excited state and after about $10^{-7} - 10^{-8}$ s, it

will de-excite by sending out a scintillation photon with a wavelength of 395 nm. These blue scintillation photons may be detected and converted into an electric signal. Specifics for the GS20 Lithium6-glass can be seen in Table 2.1.

Table 2.1: Specifics for GS20 Lithium6-glass [18].

Isotopic Ratio	95% ^6Li
Total Lithium	6.6%
Density	2.50 g/cm ³
Decay time neutron excitation	57 ns
Decay time alpha excitation	49 ns
Wavelength of maximum emission	395 nm
Refractive index at maximum emission	1.55

2.2 Photomultiplier tubes

2.2.1 Single anode

The earliest use of a scintillator for particle detection was in 1903 by Crookes [17]. Today it is one of the most common detector media. In the beginning, the human eye was used to register the light flashes. In 1944, the PMT was invented to register the light flashes and today this device has completely replaced the human eye for the detection of scintillation-light flashes. Figure 2.2 shows a scintillator coupled to a PMT.

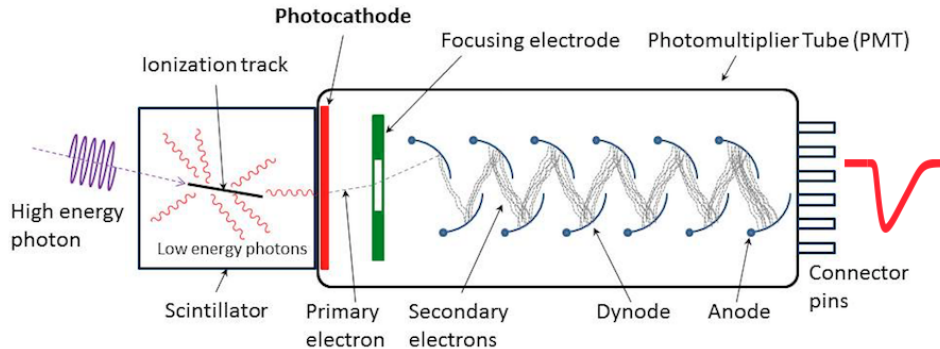


Figure 2.2: Scintillator coupled to a PMT. The incoming radiation, in this case a high-energy photon, creates scintillation photons which interact with the photocathode and result in a photoelectron. This photoelectron is multiplied after interaction with the dynodes. The signal is read out at the anode and is proportional to the energy of the incoming radiation. The red pulse represents the resulting signal. Figure from [20].

The scintillation photons enter into the photocathode through the optical window. They free photoelectrons via the Photoelectric Effect at the photocathode [15]. These photoelectrons are then focused by an electrode and accelerated towards the first dynode. When hitting the first dynode, the photoelectrons transfer some of their energy to the electrons in the dynode. This causes secondary electrons to be released, which in turn are focused and accelerated towards the next dynode. This process is repeated at each dynode and results in an amplification of the incoming electrons with a factor of around a million. The final charge is then collected at the anode and is proportional to the energy of the incoming radiation.

2.2.2 Multi anode

One drawback with a single anode PMT is that it cannot measure the spatial distribution of the incoming radiation. It does not matter where the incoming photon strikes the photocathode, all the electrons created are directed towards a single electron-multiplier unit. To measure the spatial distribution of the incoming radiation, MaPMTs have been developed. The MaPMT is conceptually equivalent to incorporating multiple single-anode PMTs into a single high-density unit. A photograph of a MaPMT is shown in Fig 2.3 and a schematic figure of a MaPMT and how the signal multiplication works is shown in Fig. 2.4.

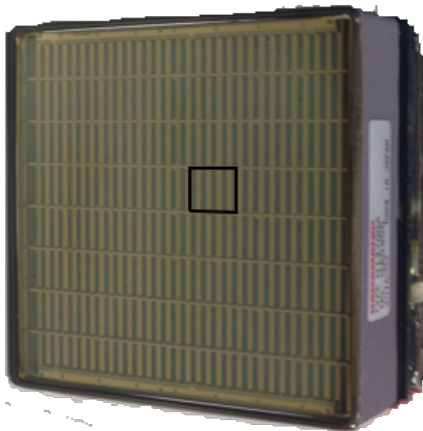


Figure 2.3: Photograph of a MaPMT. Each square on the surface corresponds to one pixel and the entire surface consists of 64 pixels.

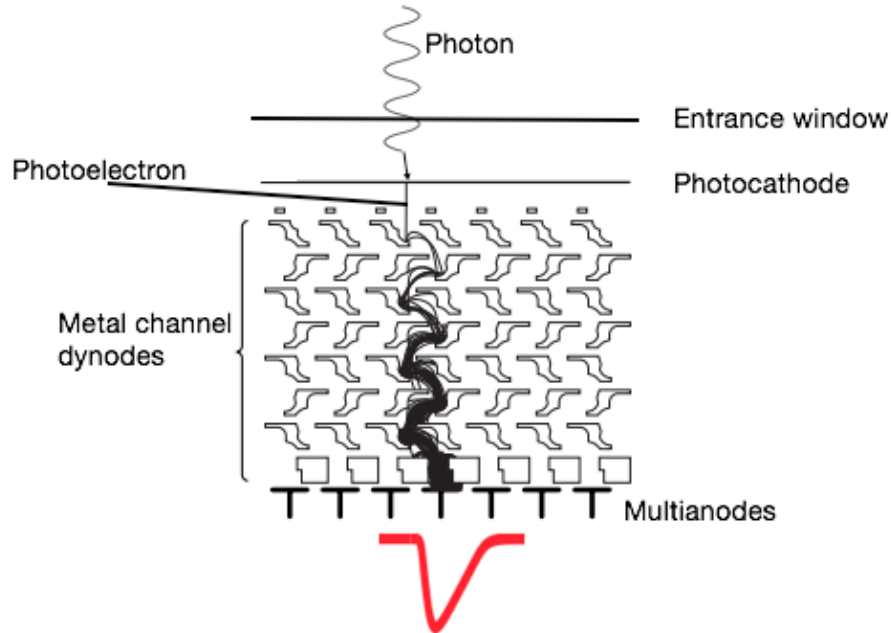


Figure 2.4: Signal multiplication within a MaPMT. The incoming scintillation photon enters through the entrance window and frees an electron in the photocathode. At each dynode, the electrons are multiplied and eventually read-out at the multi-anode. The red pulse at the bottom represents the resulting signal on the anode the shortest distance from the production site of the photoelectron. Figure from [21].

Dynode 12 is the linear OR of signal from all 64 anodes. It is provided for self-triggering purposes, see Sec. 2.5.1. During this work, the H8500C MaPMT [22] from the Japanese company Hamamatsu will be used. It has 64 pixels, where one pixel is the same as one PMT. Details about the H8500C MaPMT can be found in Table 2.2.

Table 2.2: Specifics for the Hamamatsu MaPMT H8500C [22].

Pixels	64
Pixel size	$5.8 \times 5.8 \text{ mm}^2$
Effective area	$49 \times 49 \text{ mm}^2$
Spectral range	300 – 650 nm
Peak wavelength	400 nm

2.3 Basic electronic concepts

2.3.1 Threshold

The minimum signal required to create a trigger is set by a discriminator and this energy value is called the threshold. Particles with energy below this threshold value will not create a trigger and therefore not be detected. It is a difficult task to select the optimal threshold value. Setting the threshold too high can lead to the loss of actual events and setting it too low can lead to events of interest being lost in the uninteresting low-energy background. In Fig. 2.5, both signals will be detected for threshold setting A while only the larger signal will be detected with threshold setting B. Discriminator thresholds can lead to the “walk” effect (see below).

2.3.2 Walk effect and constant-fraction discriminator

As can be seen in Fig. 2.5, there will be a difference in start time between the two signals for threshold setting A due to the signals having different amplitudes. This is called the walk effect and it is generally difficult to correct for in the data analysis. In the optimal case, the amplitude of the signal should not affect the timing. One solution to correct for the walk effect is to use a constant-fraction discriminator (CFD). Figure 2.6 shows the principle of a CFD. The analog input signal is split and one portion is delayed while the other is inverted before they are summed together again. The trigger is now defined by the zero-crossing point of the summed signal, which can be used for walk-free timing.

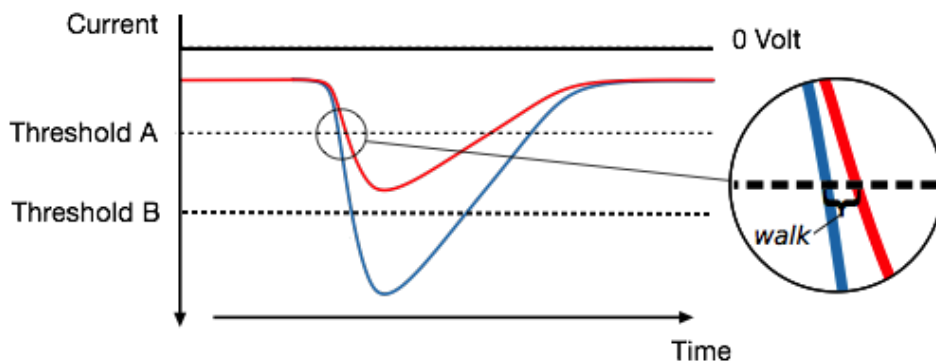


Figure 2.5: QDC discriminator settings and the walk effect. For threshold setting A, both signals will be detected but for threshold setting B, only the one with larger amplitude (blue) will be detected. For threshold A, there will be a time difference between the two start times due to the different amplitudes. Figure from [23].

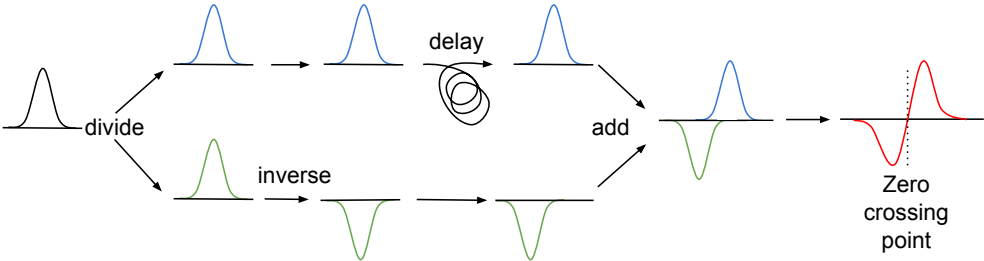


Figure 2.6: Constant-fraction discriminator principle. The input signal (black) is split into two (green and blue). The blue signal is delayed and the green is inverted before being summed together. The trigger timing is now defined by the zero-crossing point, which is amplitude independent. Figure from [23].

2.3.3 Time-to-digital converter

A time-to-digital converter (TDC) is a device which is often used to measure the time at which an event occurs relative to a common start. A TDC may measure time by counting the number of oscillations of a crystal vibrating with a known stable frequency [15]. The relative timing obtained can then be used to identify interesting events or distinguish between multiple events which occur at different times in the same detector.

2.3.4 Charge-to-digital converter

A charge-to-digital converter (QDC) is a device that can integrate current to yield the charge, see Eq. 2.2.

$$Q = \int_{T_{start}}^{T_{stop}} i(t) dt \tag{2.2}$$

Histogramming the result of this integration produces a spectrum containing both a “pedestal” and a peak from the real events, see Fig. 2.7.

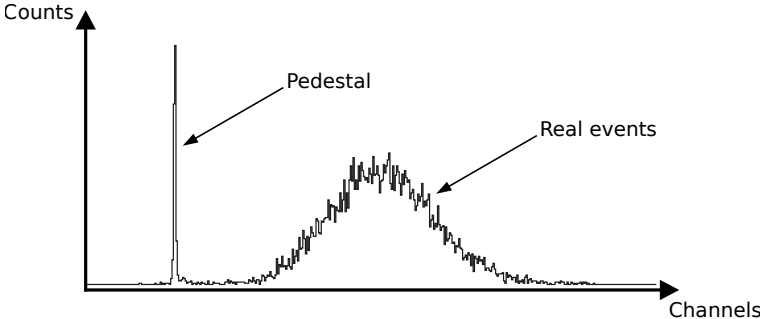


Figure 2.7: QDC spectrum. The sharp peak to the left is the pedestal while the wider peak to the right corresponds to real events.

The integral of a current pulse from a PMT is equal to the charge produced by the event, which in turn is proportional to the energy deposited in the detector by the event. When the gate opens at T_{start} , the QDC starts the integration and when the gate closes at T_{stop} , the integration stops. The concept can be seen in Fig. 2.8.

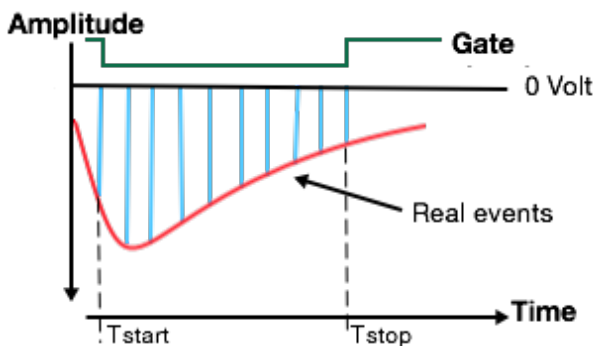


Figure 2.8: QDC concept. The red pulse represents the signal coming from a PMT. The integration gate opens at T_{start} and closes at T_{stop} . The blue area is the charge, which is proportional to the energy deposited in the detector.

When a particle hits any pixel in a MaPMT, there will be a single common gate generated for all the QDCs attached to all of the pixels. This leads to pixels which did not register an event integrating their electronic offset from ground to give a pedestal count, see Fig. 2.9. Thus, the pedestal peak in the QDC spectrum represents the location of zero-energy events.

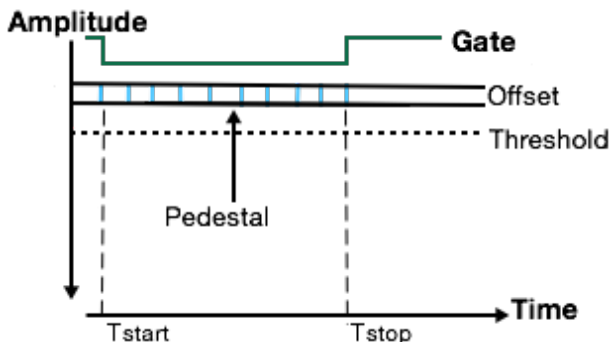


Figure 2.9: QDC pedestal concept. A signal is detected in another pixel. A common gate generated by that pixel results in an integration from T_{start} to T_{stop} in this pixel. Since there is no signal in this pixel, the integration will determine the charge in the offset region, resulting in a pedestal, or zero-energy event. Figure from [23].

2.4 Hamamatsu calibration data sheet

As mentioned in Sec. 2.2.2, the MaPMT which will be used is the Hamamatsu H8500C. During production, efforts are made to ensure that the responses of the pixels are as equal as possible but small variations will still occur. These variations need to be understood. Hamamatsu provides a calibration data sheet for each separate unit they manufacture. This data sheet reports the so-called relative gain for each of the pixels, see Table 2.3.

Table 2.3: Relative gain for each pixel/QDC from Hamamatsu data sheet

QDC	Pixel	Gain	QDC	Pixel	Gain	QDC	Pixel	Gain
0	1	0.83	22	27	0.77	43	46	0.88
1	2	0.81	23	28	0.79	44	53	0.95
2	9	0.76	24	35	0.80	45	54	0.93
3	10	0.68	25	36	0.85	46	61	0.95
4	17	0.77	26	43	0.90	47	62	0.98
5	18	0.76	27	44	0.89	48	7	0.95
6	25	0.76	28	51	0.90	49	8	0.92
7	26	0.78	29	52	0.89	50	15	0.79
8	33	0.79	30	59	0.89	51	16	0.87
9	34	0.80	31	60	0.91	52	23	0.81
10	41	0.84	32	5	1.00	53	24	0.91
11	42	0.82	33	6	0.99	54	31	0.83
12	49	0.85	34	13	0.82	55	32	0.93
13	50	0.81	35	14	0.78	56	39	0.85
14	57	0.89	36	21	0.81	57	40	0.96
15	58	0.86	37	22	0.85	58	47	0.88
16	3	0.82	38	29	0.83	59	48	0.98
17	4	0.89	39	30	0.87	60	55	0.89
18	11	0.72	40	37	0.87	61	56	0.98
19	12	0.76	41	38	0.90	62	63	0.96
20	19	0.76	42	45	0.92	63	64	0.88
21	20	0.78						

The data sheet was produced using a W-Lamp [24] with blue filter (DC Light) illuminating the MaPMT, see Fig. 2.10.

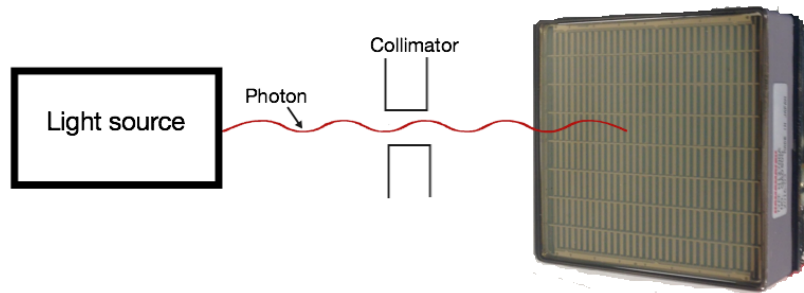


Figure 2.10: Hamamatsu test setup. The photon (red) comes from the W-lamp and illuminates one pixel of the MaPMT.

The spot illuminated was restricted to $6 \times 6 \text{ mm}^2$ and spatially matched to the pixel with a collimator. The voltage used was -1000 V .

In this section, the concept of gain will be discussed in detail.

2.4.1 Pedestal correction and fitting

The values that are obtained in Table 2.3 are determined by illuminating one pixel of the MaPMT at a time. The spectra from the illumination are then pedestal corrected and gain matched. In this section, the procedure is explained in detail.

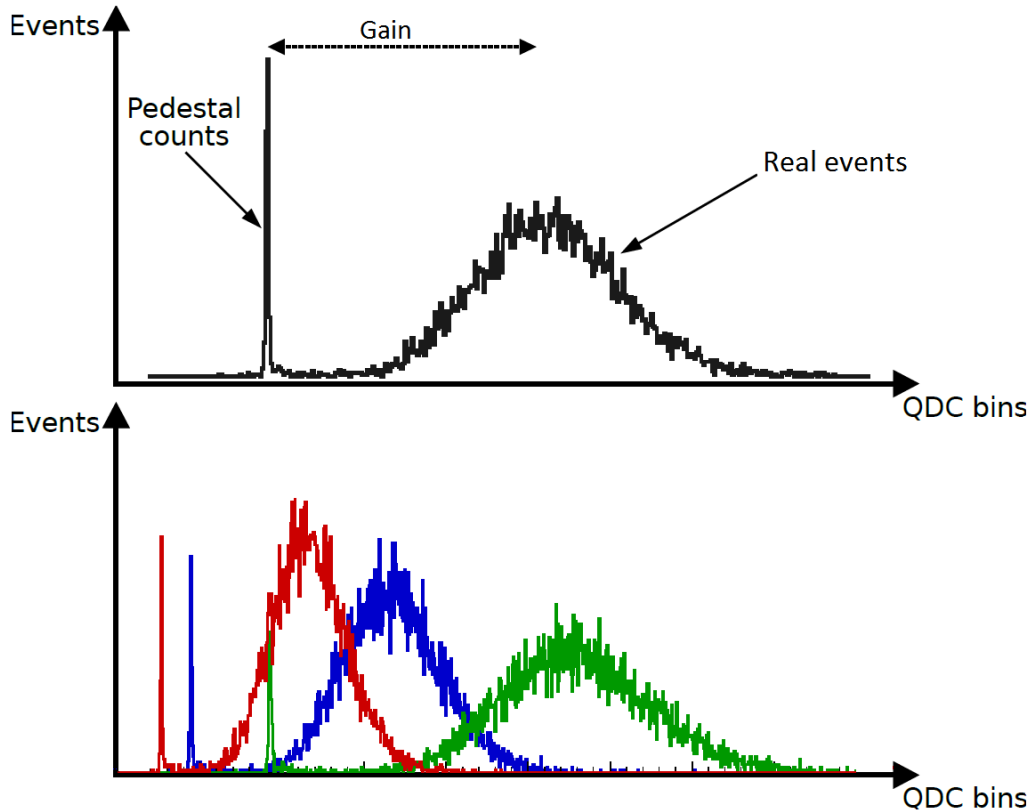


Figure 2.11: QDC spectra. Top panel: a single spectrum with the pedestal peak to the left and the counts from real events to the right. The distance between these peaks is the gain. Bottom panel: three QDC spectra, where the red, blue and green distributions represent different pixels, each having different pedestals and different gains.

The top panel in Fig. 2.11 shows a typical gain spectrum obtained for one pixel. In the bottom panel, the spectra for two additional pixels have been superimposed. The pedestals end up at different positions in the bottom figure due to pixel-to-pixel variations in the signal-processing electronics.

The first step towards understanding the gain presented in the Hamamatsu data sheet is to perform a pedestal correction, see the top and middle panels in Fig. 2.12.

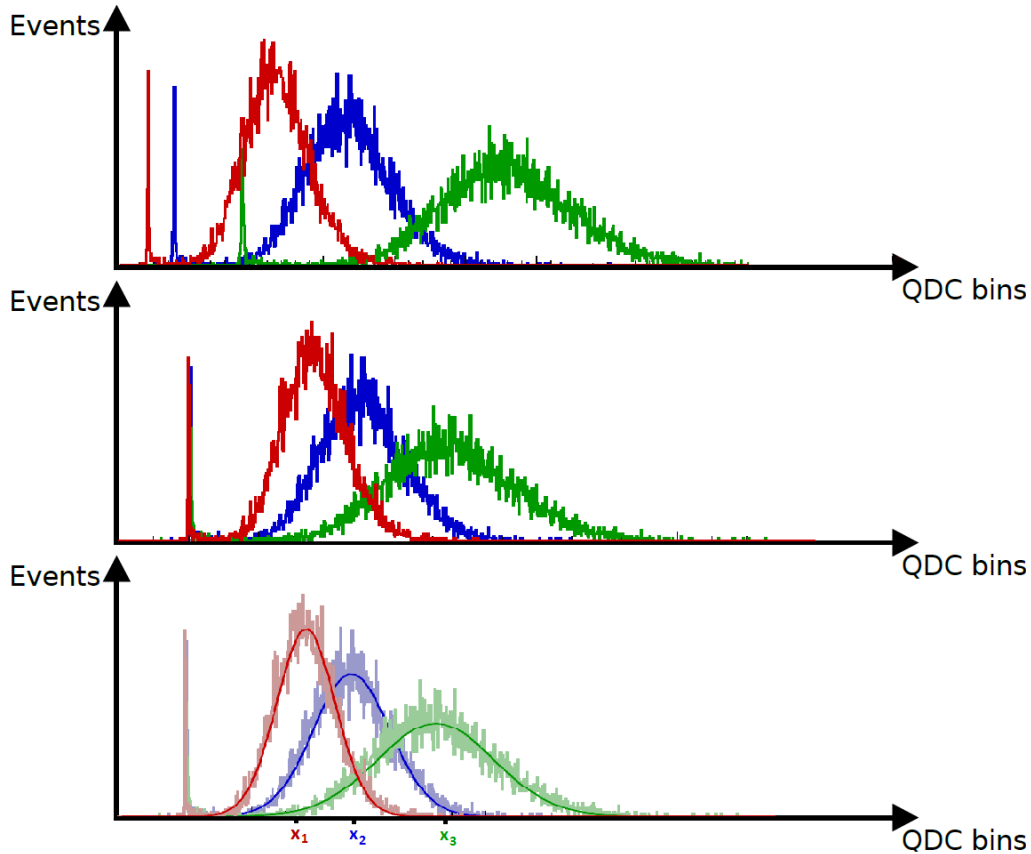


Figure 2.12: Pedestal correction and Gaussian-fitting procedures. Top panel: Same figure as bottom panel in Fig. 2.11. Middle panel: Pedestal corrections have been performed, resulting in the same zero-energy point for each spectrum. Bottom panel: Gaussian fits have been applied to determine the peak locations for each spectrum.

Pedestal correction refers to the position of a spectrum along the x-axis being modified according to the location of the zero-energy point (pedestal). In the top panel of Fig. 2.12, three different spectra corresponding to three different pixels with three different pedestals and three different gains are shown. The middle panel illustrates the three different spectra after the pedestal correction. All three have been shifted to a common zero-energy point, which allows for meaningful comparison of the gain variation. A Gaussian is then fitted to the real-event distribution for each of the channels, see the bottom panel in Fig. 2.12. The locations of the peaks x_1 , x_2 and x_3 derived from the Gaussian fit functions are then used to produce the relative gain matrix.

The Gaussian gain-fitting procedure is illustrated in Fig. 2.13.

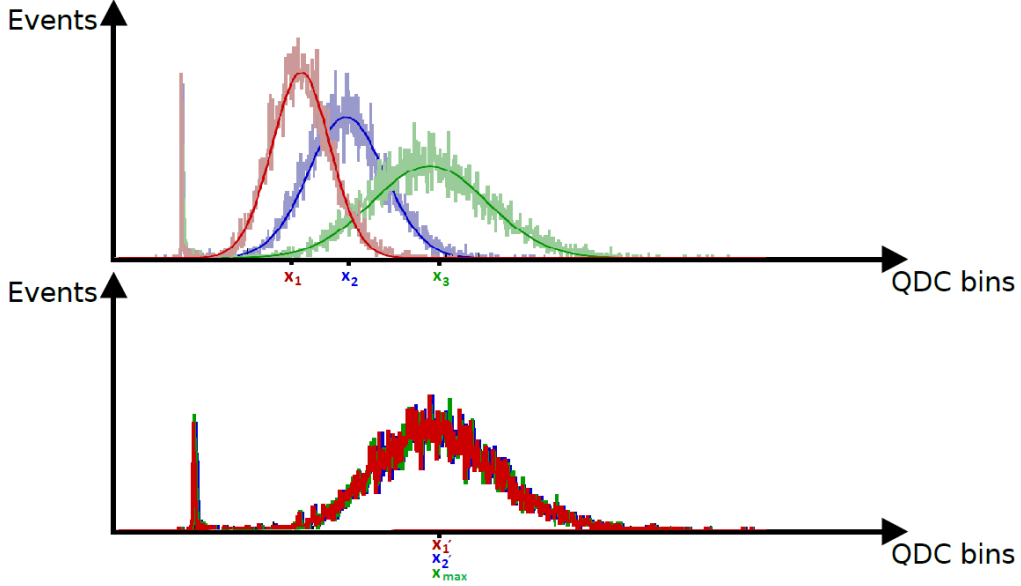


Figure 2.13: Gaussian gain-fitting procedure. Top panel: Same figure as bottom panel in Fig. 2.12. Bottom panel: The three spectra have been gain matched using software.

The gain matching, and thereby the calculation of the corresponding gain coefficients, is done in such a way that the distributions from all pixels are scaled to match that from the pixel with the highest mean value x_{max} , see Eq. 2.3.

$$\text{Relative gain coefficient}|_i = \frac{\text{Peak location for pixel}|_i}{\text{Highest peak location of all pixels}} = \frac{x_i}{x_{max}} \quad (2.3)$$

For example, in Fig. 2.13, the blue and red spectra are fitted and then matched to the green spectrum via the relative gain coefficients determined using Eq. 2.3 in an offline analysis on an event-by-event basis. That is, the relative gain coefficient for the pixel corresponding to the red spectrum is calculated by dividing the mean value x_1 of the red Gaussian with the mean value x_3 of the green Gaussian. Each event in the red spectrum in the top panel of Fig. 2.13 is then scaled by the inverse of this relative gain coefficient one at a time, and the results binned accordingly.

The meaning of the gain coefficients for all MaPMT pixels presented in Table 2.3 should now be clear. For example, suppose pixel 5 has the highest gain and pixel 54 has a gain which is 86% of this highest gain. In order to compare spectra obtained using the two pixels, the spectrum corresponding to pixel 54 must first be corrected by the relative gain variation, $1/0.86$, on an event-by-event basis.

2.5 Measurements

2.5.1 Test bench at the University of Glasgow

A schematic overview of the test-bench setup used to perform the characterization for this thesis can be seen in Fig. 2.14.

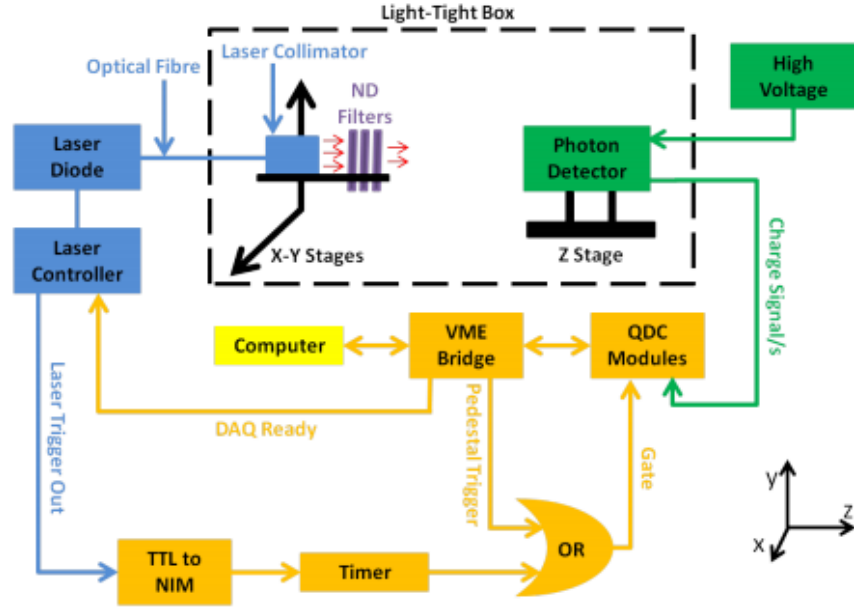


Figure 2.14: Test-bench setup at the University of Glasgow. The laser and/or source is mounted on motorized X - Y stages enabling scanning across MaPMT surfaces with a minimum step size of $1 \mu\text{m}$. Figure from [25].

The test bench consists of a light-tight box, an optical table and standard VME electronics used to read out the signals from each of the 64 MaPMT pixels separately [26]. Each QDC contains 32 channels and thus 2 modules were needed. The analogue signal from the MaPMT was extracted using a custom-made readout board, which had one common ground line among all channels, and transferred to the QDC. On this custom-made readout board, there is the possibility of extracting the signal for each pixel separately as well as the possibility to extract the common dynode 12 signal.

The setup used for reading out the dynode 12 signal with the test bench setup can be seen in Fig. 2.15.

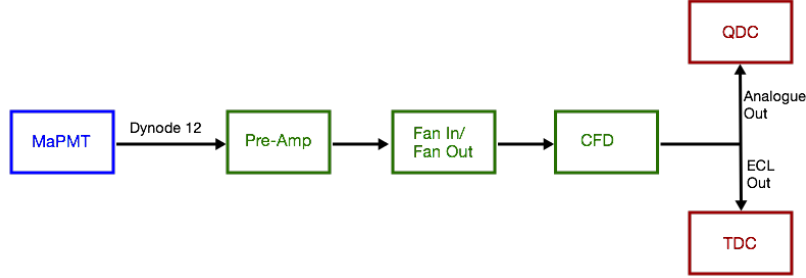


Figure 2.15: Setup used for reading out the dynode 12 signal. Figure from [25].

The dynode 12 signal from the MaPMT is first amplified with an ORTEC FTA820 Pre-Amp and then inverted from positive polarity to negative polarity with a LeCroy Fan In/Fan Out module. The inverted signal is then discriminated with a CFD. The optional analogue output signal from the CFD is sent to the QDC (same QDC as for the signals from the individual channels) and the Emitter-Coupled Logic (ECL) output signal is sent to a TDC.

2.5.2 Laser irradiations

The laser setup consists of two PiLas EIG1000 picosecond lasers with wavelengths of either 407 (blue) or 635 (red) nm and variable beam diameter [27]. The laser diode and control unit are placed outside a light-tight box and the laser light is transported into the optical box via an optical-fibre cable and focused by a collimator.

The collimator is mounted on X – Y motorized stages. The two motorized stages are Thorlabs NRT150 precision motors, one for horizontal and one for vertical movements. This in turn makes it possible to scan across the entire surface of the MaPMT. The minimum step size is $0.1 \mu\text{m}$ with a step accuracy of 5% [28]. To get the desired light level, absorptive Neutral Density Filters (NDFs) from Kodak were used to attenuate the intensity of the laser beam. The NDFs were placed directly on the laser collimator.

The trigger signal for the laser was generated with the help of a CAEN V2718 VME Bridge connected to a computer. Before emitting the light pulses, the laser controller generated a Transistor-Transistor logic Logic (TTL) trigger signal. The signal was reshaped with a CAEN N89 Nuclear Instrumentation Module (NIM)/TTL converter and stretched by a CAEN N93B Dual Timer before it was used as the gate signal for the CAEN V792 QDCs.

The MaPMT was used with the Lithium6-glass scintillator mounted with the help of silicon gel. The voltage to the MaPMT was set to -1000 V and the

MaPMT was placed on a stand at the focal spot of the laser, see Fig. 2.16.

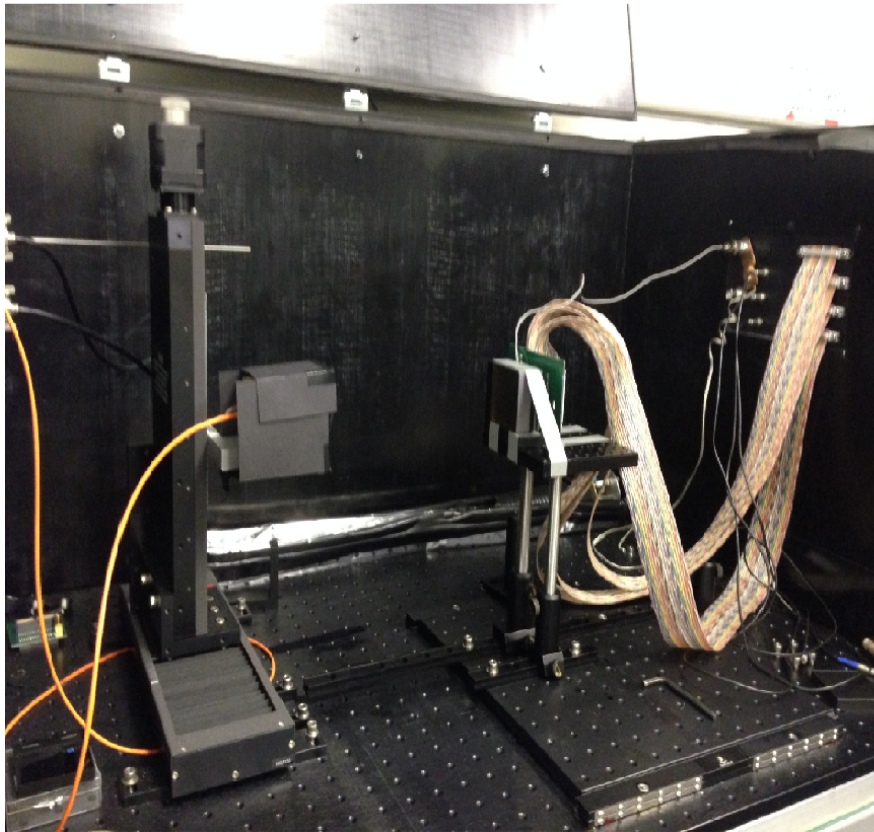
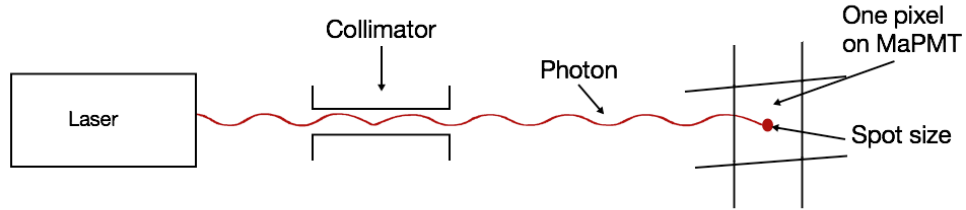


Figure 2.16: Setup for laser measurements. Top panel: a laser photon passes through the collimator and strikes a pixel of the MaPMT. Bottom panel: a picture of the setup. The MaPMT is mounted on a stage 180 mm from the laser collimator.

The distance between the laser and its focal spot was determined using a Hamamatsu Charge-Coupled Device (CCD) camera, model C9260-901. The CCD camera was placed at three different distances from the laser: 100 mm, 180 mm and 250 mm. The CCD camera was used to confirm that the intensity of the laser

is the highest and the beam size is the smallest when placed 180 mm from the laser. The beam size was measured to be between 100-150 CCD pixels. One CCD pixel is $6.45 \times 6.45 \mu\text{m}^2$ [29] and the size of the entire beam is therefore 0.65-1.0 mm in each direction. This assures that the beam only strikes one MaPMT pixel at a time since the size of each MaPMT pixel is $5.8 \times 5.8 \text{ mm}^2$, see Table 2.2.

A central scan test was performed twice (the second time for reproducibility, see Sec. 3.1.1). Central scan test means that the laser fires ten thousand photons into the center of a pixel before moving on to the next one. The starting point has to be set manually and is preferred to be in the middle of each pixel to assure that the laser only irradiates one pixel at a time. The red laser, with the wavelength 635 nm, was used with a frequency of 1 kHz with the tune (intensity) set to 50%. A NDF with the value of 1.5 was placed in front of the laser collimator as fine tuning to produce the desired intensity of red laser light. The results of the measurements are presented in Sec. 3.1.

2.5.3 Alpha-particle irradiations

During the alpha-irradiation measurements, a thin-windowed Americium241 alpha source was used. Americium241 has atomic number 95 and is no longer naturally occurring. It has to be produced from plutonium. The half life is 432.2 years. Its main decay is via alpha decay to Neptunium237 and gamma-rays, see Fig 2.17 for the complete alpha-decay chain. As can be seen in Fig 2.17, the main alpha-particle energy α_3 is 5.486 MeV (about 85% of the time) and thus the main gamma-ray energy γ_4 is 59.5 keV.

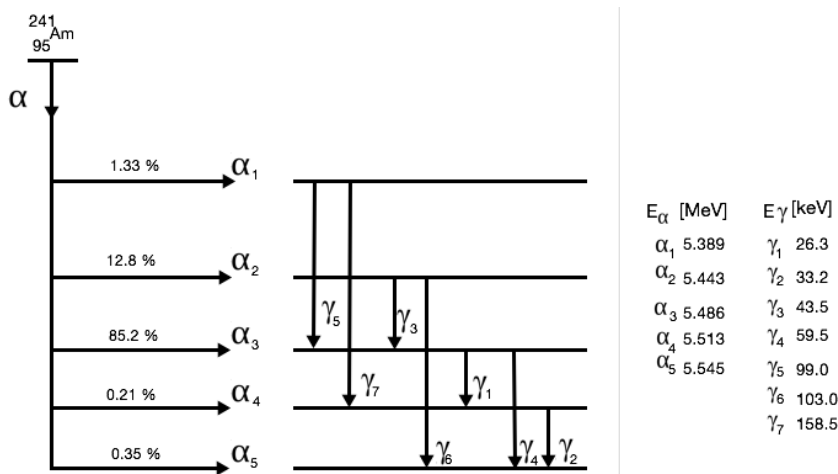


Figure 2.17: Americium241 decay to Neptunium237. The main alpha-particle energy is 5.486 MeV and the main gamma-ray energy is 59.5 keV. Figure from [30].

As the alpha particles travel through different materials, they lose energy. For air, alpha particles with energy 5.48 MeV travel 4.05 cm [31]. During the measurements, the alpha source was positioned 1.5 cm from the detector. The alpha particles hitting the Lithium6-glass scintillator therefore have an energy of around 3.5 MeV. The range of 2.05 MeV alpha particles in Lithium6-glass is $5.3 \mu\text{m}$ [32]. The range for 3.5 MeV alpha particles will therefore be about $10 \mu\text{m}$ in Lithium6-glass, see Fig. 2.18.

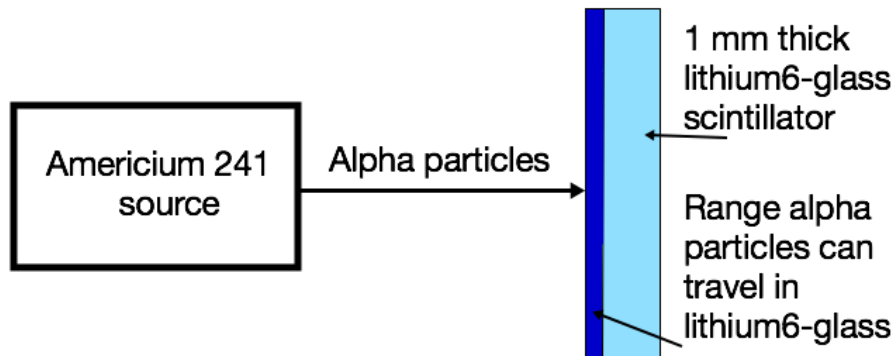


Figure 2.18: Range of alpha particles in Lithium6-glass. The energy of the alpha particles when emitted from the source is 5.48 MeV. When they arrive at the glass, the energy is around 3.5 MeV which gives a range of about $10 \mu\text{m}$ in the glass. Thus, it is only the upstream surface of the Lithium6-glass scintillator which is irradiated.

For the alpha measurement, a thin-windowed Americium241 source was placed on top of the motor inside the optical box. The MaPMT, with the Lithium6-glass scintillator in place, was positioned 1.5 cm from the source to minimize alpha-particle energy losses in the air. The source was collimated with a 2 mm thick sheet of lead with a 2 mm hole, see Fig. 2.19.

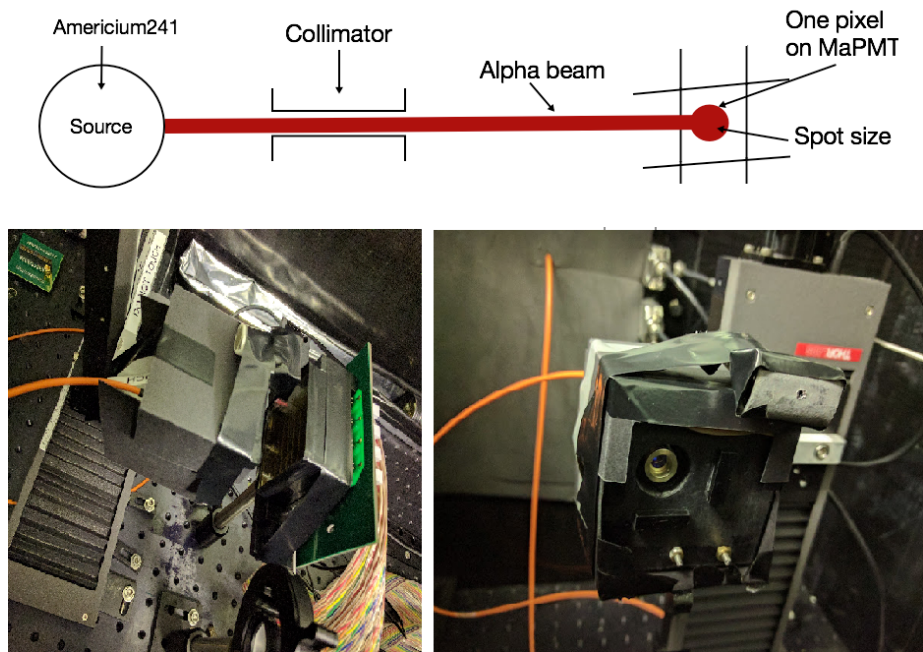


Figure 2.19: Setup for alpha-particle measurements. Top panel: the alpha-particle beam emitted from the Americium241 source irradiates one pixel of the MaPMT. Bottom panel: Photographs showing how the alpha source was placed on top of the laser collimator in the test-bench setup.

The dynode 12 signal was used to trigger the data-acquisition system. It was inverted and amplified by a factor two before being delayed by 32 ns and then converted to a logic signal. The discriminator performing the conversion had a threshold set to -15.10 mV. The logic signal was then sent to a OR-module and connected to a gate generator, see Section 2.5.1. The 32 ns delay from the delay module combined with all cables used gave a total delay for the gate of 100 ns. The gate width was 200 ns. The MaPMT signal was thus delayed by 200 ns with a delay box for it to arrive within the gate signal. A single central scan was performed on the MaPMT at -1000 V for 10k events per pixel.

The results of the measurements are presented in Sec. 3.2.

Chapter 3

Results and discussion

3.1 Calibration gain maps

3.1.1 Reproducibility test

A reproducibility test for the response of the detector prototype to the laser light was performed. The calibration derived from the first laser central scan measurement was tested against the second laser central scan measurement, see Fig. 3.1.

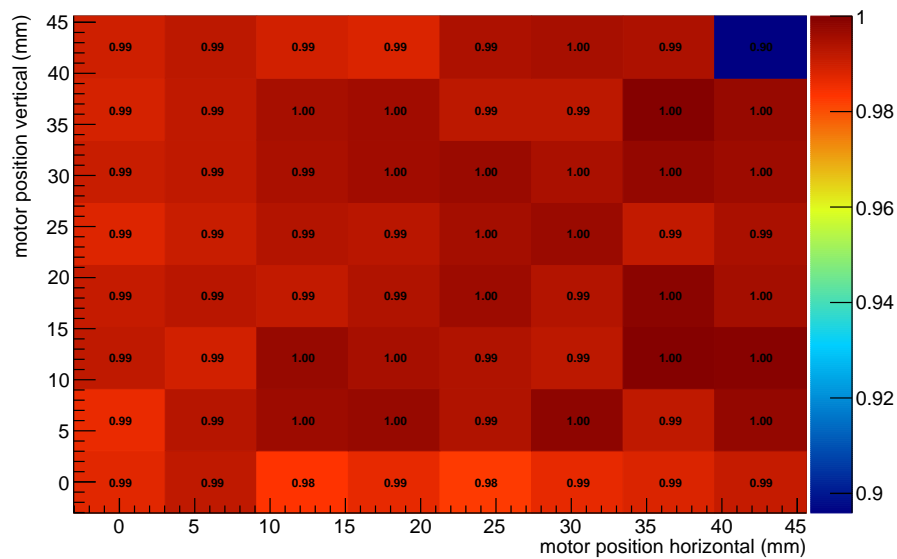


Figure 3.1: Normalized reproducibility test. The gain map derived from the first laser measurement was tested against the second laser measurement. A value of unity indicates complete reproducibility. The blue pixel was problematic.

The second measurement employed exactly the same settings as the first. The spectrum obtained from the second measurement was not modified in any way when the calibration from the first measurement was applied. The gain coefficient for each pixel obtained from the first measurement was directly applied to the data obtained for each pixel obtained during the second measurement. This results in new gain values for each of the pixels from the second measurement. These run2 values were then normalized to the run1 values.

Figure 3.1 presents an overview of the result. A value of unity indicates complete reproducibility. All pixels registered either 0.99 or 1.00 except the top right pixel, which registered 0.90. This indicates that the gain in run2 for this pixel was substantially lower than the gain for this pixel in run1, which likely indicates a hardware issue such as failure. That said, the gain characteristics of 63 out of 64 pixels were highly reproducible.

Even though the CCD camera confirmed that the laser beam only irradiated one MaPMT pixel at a time, there were clearly pulses detected in the adjacent pixels. During the reproducibility test, a light leakage or “glow” effect of around 7% into adjacent pixels was noticed, see Fig. 3.2.

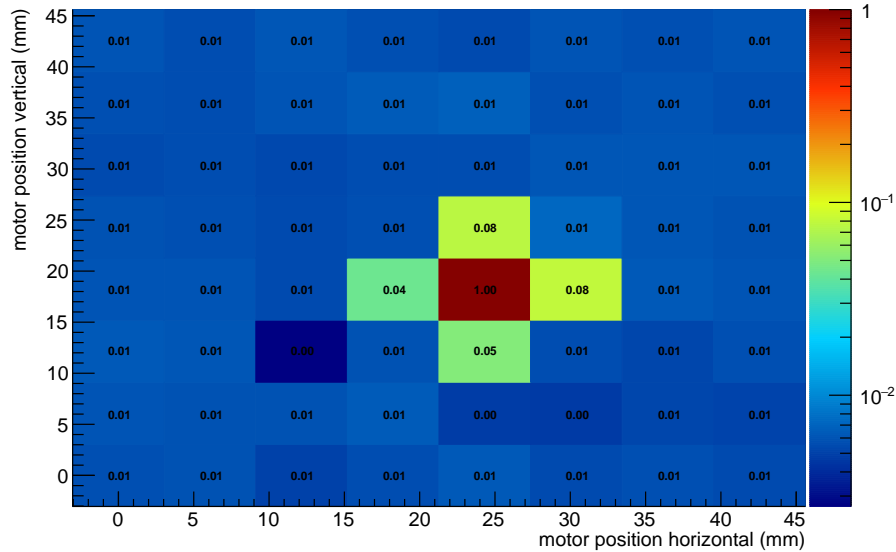


Figure 3.2: Laser gain map for pixel 29/QDC 38. The adjacent pixels also register pulses. This is due to scintillation light leakage.

Figure 3.3 shows QDC spectra for the irradiated pixel, a pixel directly above the irradiated pixel, and a pixel once more removed above the irradiated pixel.

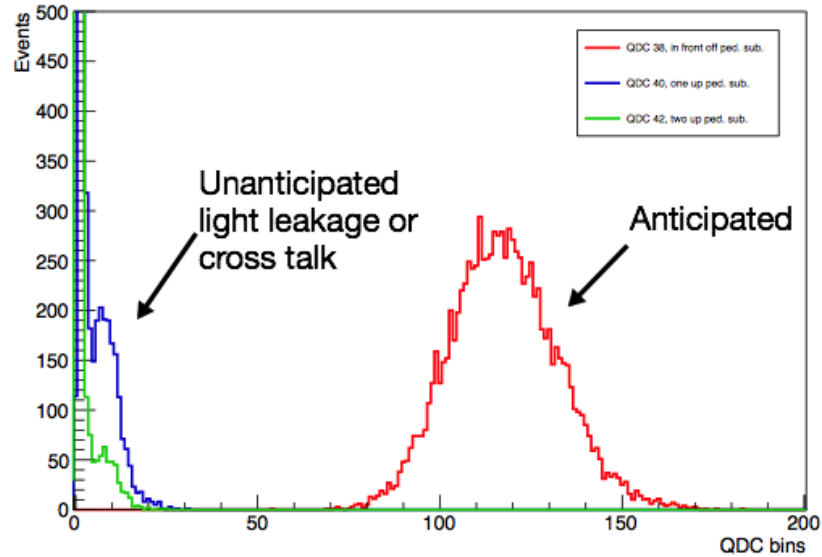


Figure 3.3: Spectra for pixel 29/QDC 38, 37/40 and 45/42. The laser irradiates the pixel corresponding to QDC 38 (red). QDC 40 (blue) is one pixel above in the y-direction and QDC 42 (green) is two pixels above in the same direction.

As can be seen, the irradiated pixel shows the anticipated distribution centered at about QDC bin 120, while the adjacent pixel and the pixel one above that show wider pedestals and an unanticipated distribution centered at QDC bin 8. The pixel directly adjacent to the irradiated pixel shows a greater response to the leaking light. This light leakage between pixels will require further investigation.

3.1.2 Hamamatsu vs. laser calibration

The gain coefficients for each pixel, both for the laser calibration and the Hamamatsu data-sheet calibration, can be seen in Table 3.1.

Table 3.1: Gains obtained from data-sheet and laser calibration. The laser calibration values were derived using the pedestal correction and gain-fitting procedure previously detailed in Sec. 2.4.1.

QDC	Pixel	Data sheet value	Laser value	QDC	Pixel	Data sheet value	Laser value
0	1	0.83	0.68	32	5	1.00	0.74
1	2	0.81	0.73	33	6	0.99	0.75
2	9	0.76	0.87	34	13	0.82	0.68
3	10	0.68	0.62	35	14	0.78	0.64
4	17	0.77	0.85	36	21	0.81	0.73
5	18	0.76	0.67	37	22	0.85	0.77
6	25	0.76	0.86	38	29	0.83	0.75
7	26	0.78	0.68	39	30	0.87	0.81
8	33	0.79	0.86	40	37	0.87	0.78
9	34	0.80	0.68	41	38	0.90	0.80
10	41	0.84	0.90	42	45	0.92	0.82
11	42	0.82	0.71	43	46	0.88	0.89
12	49	0.85	0.97	44	53	0.95	0.91
13	50	0.81	0.77	45	54	0.93	0.88
14	57	0.89	1.00	46	61	0.95	0.76
15	58	0.86	0.77	47	62	0.98	0.78
16	3	0.82	0.68	48	7	0.95	0.79
17	4	0.89	0.71	49	8	0.92	0.83
18	11	0.72	0.62	50	15	0.79	0.64
19	12	0.76	0.65	51	16	0.87	0.67
20	19	0.76	0.82	52	23	0.81	0.69
21	20	0.78	0.71	53	24	0.91	0.68
22	27	0.77	0.75	54	31	0.83	0.80
23	28	0.79	0.73	55	32	0.93	0.72
24	35	0.80	0.77	56	39	0.85	0.84
25	36	0.85	0.77	57	40	0.96	0.74
26	43	0.90	0.92	58	47	0.88	0.87
27	44	0.89	0.84	59	48	0.98	0.75
28	51	0.90	0.93	60	55	0.89	0.82
29	52	0.89	0.87	61	56	0.98	0.81
30	59	0.89	0.78	62	63	0.96	0.81
31	60	0.91	0.76	63	64	0.88	0.49

To present a more intuitive visualization of the results, the values for each calibration method are presented as gain maps, see Fig. 3.4.

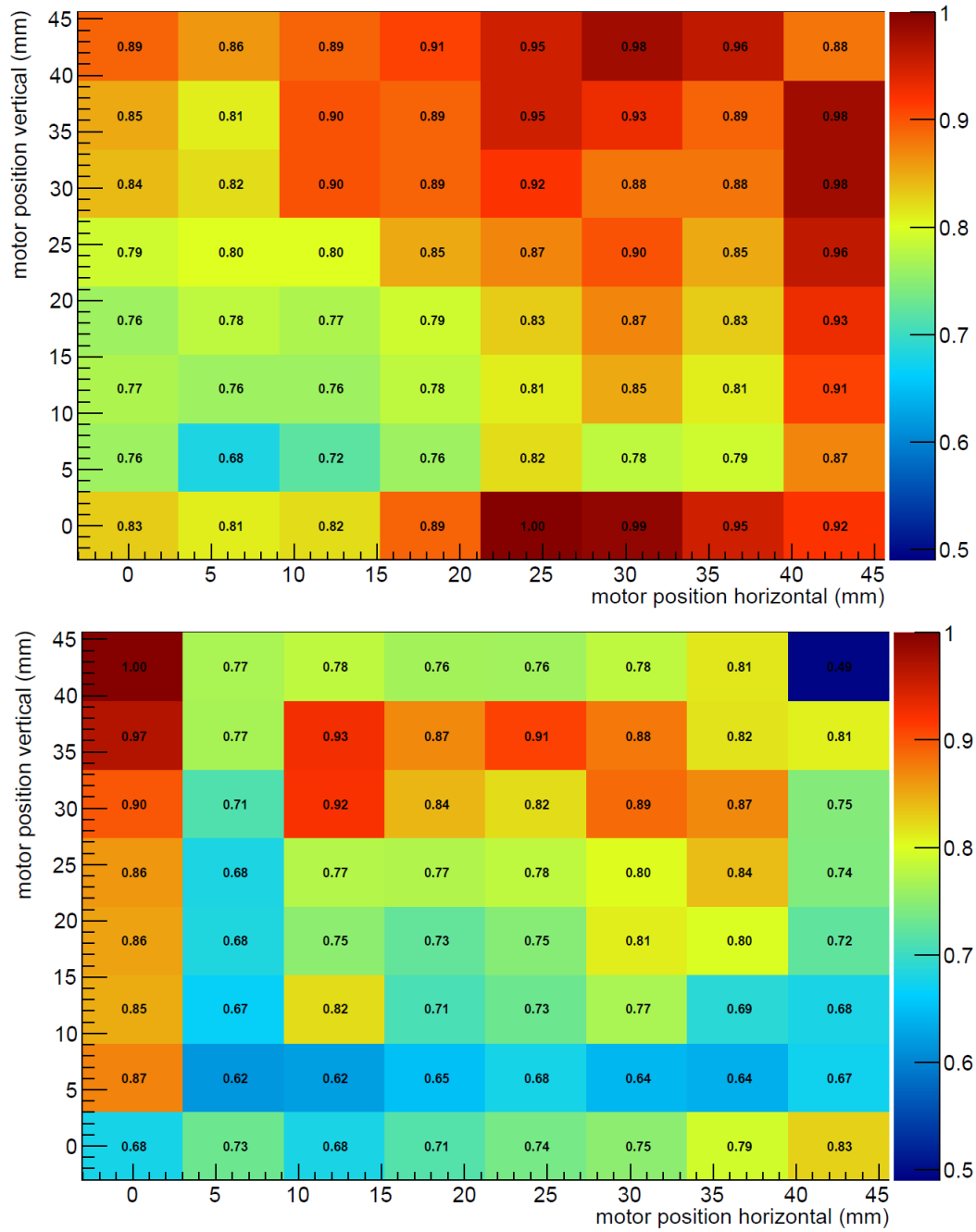


Figure 3.4: Visualization of the gain maps for both calibrations. The data presented correspond to those presented in Table 3.1. Top panel: gain map with the gain coefficients from the Hamamatsu data sheet. Bottom panel: gain map with the gain coefficients derived from the laser measurement. Clear differences exist.

The top panel shows the values from the Hamamatsu data sheet gain calibration while the bottom panel shows the values from one of the laser-calibration measurements. In both cases, the results have been normalized to the pixel with the highest gain. Note that this is not the same pixel in both cases. Normalizing to the pixel with the highest gain leads to the differences in values shown in Fig. 3.4. While the practice of normalization to the pixel with the highest gain may be debatable in the region of high-light yield studied in this thesis, it is accepted practice. The software employed here was originally developed for low light-yield applications such as Ring Imaging Cherenkov detectors where the photoelectron distributions are strictly Poisson in nature and not Gaussian. We thus chose to proceed via standard methods so that we could better compare our results to existing results. As previously mentioned, the top right pixel in the gain map for the laser calibration shows results which are suspicious, and may be a failing pixel. Generally speaking, the values from the Hamamatsu data sheet are more uniform than those corresponding to the laser-calibration measurement. This may result from Hamamatsu more uniformly illuminating the entire pixel while the laser measurements only illuminated a very small region in the center of the pixel allowing for local variations in the response of the pixel to play a role.

Figure 3.5 shows the differences between the gain coefficients displayed in Fig. 3.4, which is derived by subtracting the gain value obtained from the laser calibration from the gain value obtained from the Hamamatsu calibration, see Eq. 3.1.

$$\text{Gain difference} = \text{Hamamatsu gain} - \text{Laser gain} \quad (3.1)$$

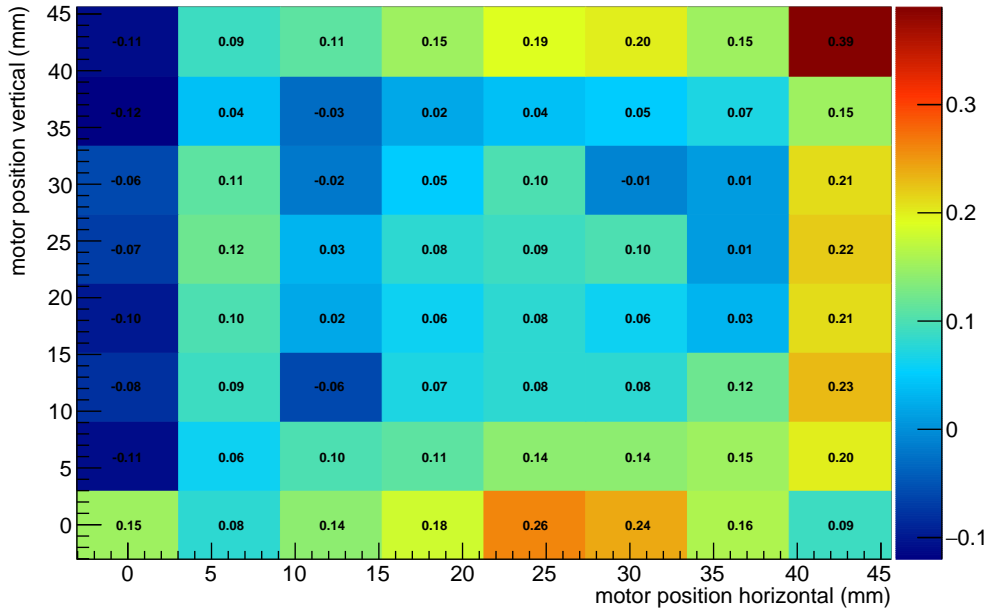


Figure 3.5: Gain differences. The number on each pixel is the gain coefficient from the laser calibration subtracted from the gain coefficient from the Hamamatsu calibration.

The gain value for the data calibration is higher for most pixels than the laser calibration since the laser calibration seems to have been performed with less incident light. Except for the suspect pixel in the top right corner, the differences between the gain values ranged from -11% to $+25\%$. With a different normalization method that considered for example the gain of the average pixel, the gain values would range from -15% to $+15\%$. Regardless of the method chosen, it is the spread in values that is of interest and it is an unexpectedly large spread. However, the fact that Hamamatsu illuminates an entire pixel as uniformly as possible while the laser was focused on a small central region of the pixel in question does not make the comparison between the gain maps completely fair. Further, note that throughout the measurements, the MaPMT and the Lithium6-glass scintillator were treated together as a single unit. It is therefore impossible to say what features in the measurements reported above are due solely to the MaPMT and what features are possibly due to scintillator effects. Since the Hamamatsu calibration data sheet is produced without having the scintillator in place, a direct comparison between that calibration and our laser calibration is also not completely fair. All this said, the differences between the calibrations were not expected to be that large. More investigations are needed.

3.2 Alpha-particle irradiation response

Recall that the goal of the SKADI project is to use SoNDe modules to detect thermal neutrons via the signature of alpha particles and tritons. As a triton beam is not readily available, a reasonable first approach to test this method of thermal-neutron detection is via alpha-particle irradiation of the prototype. A central scan of the MaPMT was thus performed using the collimated alpha-particle beam previously described to establish the response of the detector to alpha particles. Table 3.2 presents the mean gain values determined from the Gaussian fit after pedestal correction for the alpha-particle measurement.

Table 3.2: Mean gain values for each pixel for alpha-particle irradiation. These values were derived using the pedestal correction and Gaussian-fit procedure previously detailed in Sect. 2.4.1.

QDC	Pixel	Gain	QDC	Pixel	Gain	QDC	Pixel	Gain
0	1	0.46	22	27	0.39	43	46	0.50
1	2	0.40	23	28	0.40	44	53	0.53
2	9	0.39	24	35	0.40	45	54	0.55
3	10	0.33	25	36	0.43	46	61	0.53
4	17	0.38	26	43	0.46	47	62	0.53
5	18	0.35	27	44	0.46	48	7	0.55
6	25	0.38	28	51	0.46	49	8	0.84
7	26	0.37	29	52	0.46	50	15	0.47
8	33	0.39	30	59	0.47	51	16	0.63
9	34	0.38	31	60	0.50	52	23	0.46
10	41	0.40	32	5	0.53	53	24	0.69
11	42	0.39	33	6	0.50	54	31	0.49
12	49	0.42	34	13	0.45	55	32	0.75
13	50	0.39	35	14	0.44	56	39	0.51
14	57	0.45	36	21	0.44	57	40	0.79
15	58	0.45	37	22	0.46	58	47	0.54
16	3	0.40	38	29	0.45	59	48	0.81
17	4	0.45	39	30	0.48	60	55	0.57
18	11	0.34	40	37	0.50	61	56	1.00
19	12	0.38	41	38	0.49	62	63	0.58
20	19	0.39	42	45	0.51	63	64	0.98
21	20	0.39						

In order to correct the alpha-particle response for pixel-to-pixel variations in the gains, both the laser gain calibration and the Hamamatsu data-sheet calibration were each applied to the alpha-particle results, see Fig. 3.6.

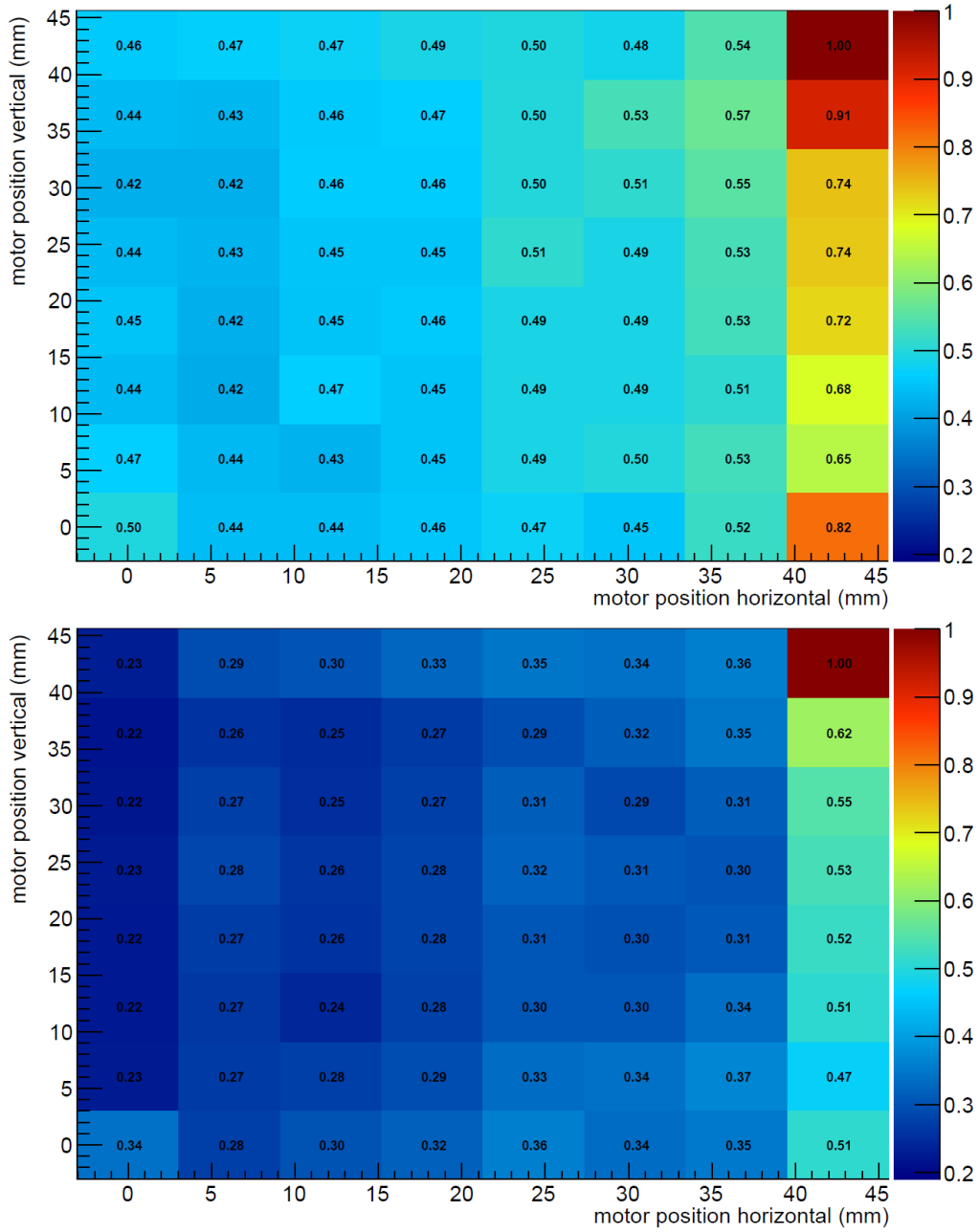


Figure 3.6: Corrected alpha-particle gain maps. Top panel: Hamamatsu calibration applied to the values in Table 3.2. Bottom panel: laser calibration applied to the same values. In both cases, the response is very uniform except for the pixels in the column furthest to the right.

The laser-reproducibility test demonstrated that the top right pixel may have failed which may explain the high value for that pixel in Fig. 3.6. The results for this pixel should be ignored. As previously discussed, the absolute magnitude of the gain variations is a strong function of the algorithm employed. Instead it is the relative values which are of interest. These relative values should be almost the same; that is, a uniform color palette was anticipated. If the color palettes were the same for both calibrations, this would mean that they could be used interchangeably.

A noticeable trend in Fig. 3.6 for both calibrations is that the values consistently increase from left to right with substantially higher values in the rightmost column. A reason for this may be that the MaPMT was slightly misaligned, see Fig. 3.7.

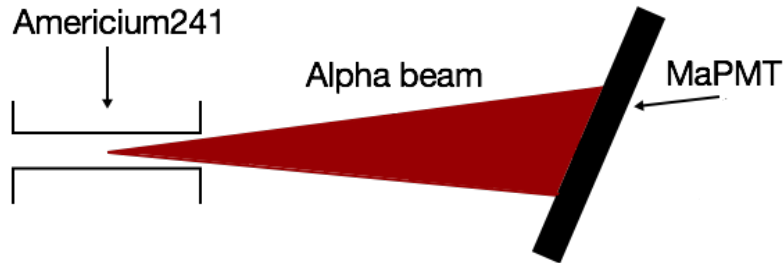


Figure 3.7: Illustration of a misaligned MaPMT. The MaPMT is seen from above and because of the misalignment, an asymmetric irradiation may have resulted.

This misalignment would not only subject one side of the MaPMT to more alpha irradiation per mm^2 but also alpha irradiation with higher energy. The combination of more alpha particles per mm^2 and higher energy per alpha particle will lead to more deposited energy and more scintillation light. The alpha particles will also ionize the air between the source and the scintillator, and this production of ions is a function of energy. This could also lead to further position-dependent pulses in the detector.

For the alpha-particle irradiation, there was no measurement of the spot size of the beam or whether it was sufficiently collimated to illuminate a single pixel at a time. Figure 3.8 shows the response of the MaPMT when collimated the alpha-particle source was placed in front of the pixel 29/QDC 38.

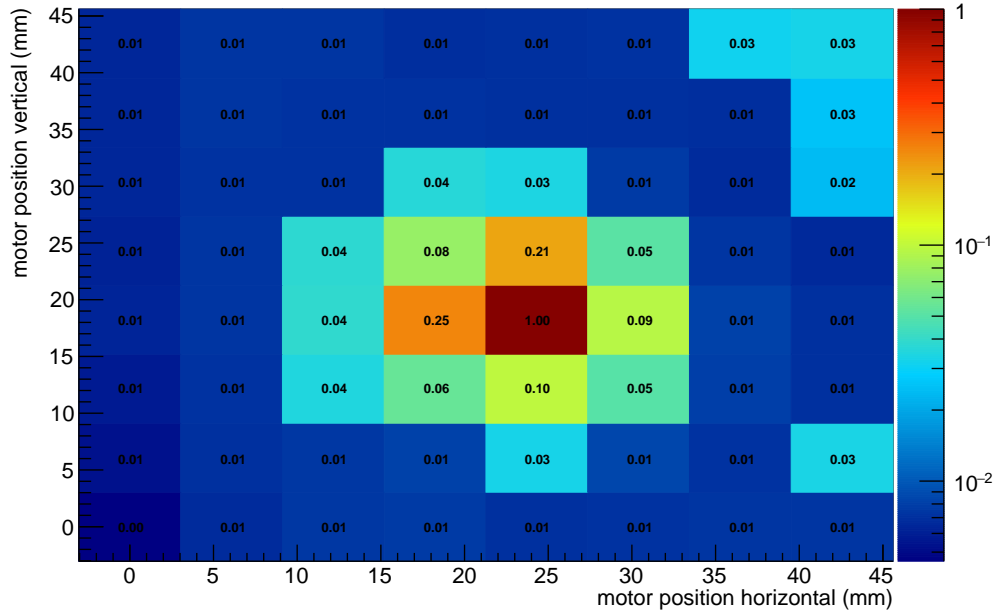


Figure 3.8: Alpha-particle gain corresponding to pixel 29/QDC 38. The collimated alpha-particle source is placed in front of QDC 38 and counts are detected in the adjacent pixels as well as in the far-right column.

The alpha-particle beam is more than twice as wide as the laser beam and a likely result of this is that more pulses are detected in the surrounding pixels. Some of the reasons for the wide spread might be that the beam was not sufficiently collimated, thereby irradiating more than one pixel at a time or that multiple scattering spread the alpha beam. It may also be that the collimator was misaligned leading to the asymmetry to the left around the irradiated pixel. It is also conceivable the collimator was not cylindrical, but rather conical. Finally, it seems the collimator may have been leaking, leading to the unexpected excess of counts in the top-right corner. Regardless, the light leakage into the adjacent pixels is around 20%, which is much higher than the laser-light leakage. More investigations are needed.

Chapter 4

Summary and outlook

4.1 Summary

The motivation for this thesis was to develop a better understanding of the response of a SoNDe-module prototype which will ultimately be used to instrument the SKADI beamline at ESS. The SoNDe-module prototype has been designed to detect thermal neutrons with high position resolution and consists of a 1 mm thick GS20 Lithium6-glass scintillator wafer mounted on a Hamamatsu H8500C MaPMT using a 1 mm thick layer of silicon optical gel. Initial characterizations of the response to laser light and a collimated alpha-particle beam were performed. A precision stepping motor test bench at the Department of Nuclear Physics at the University of Glasgow was employed. A 0.8 mm diameter collimated red laser (635 nm) and a 2 mm diameter collimated alpha-particle beam from a thin-windowed Americium241 source were used in the studies. The center of each pixel of the SoNDe-module prototype was irradiated. The data were acquired using a NIM/VME-based data-acquisition system and analyzed within the ROOT framework. The datasets obtained include a laser-irradiation reproducibility study and an attempt to recreate the gain calibration data sheet provided by Hamamatsu together with a first-ever study of the response of the SoNDe-module prototype to alpha particles. The study of the alpha-particle response was envisioned as the first step towards the study of the response to thermal neutrons.

The response of the SoNDe-module prototype to a central scan of red laser light was demonstrated to be reproducible on a pixel-by-pixel basis to the level of 1%. Leakage of scintillation light into adjacent pixels at the level of about 7% was observed. The absolute gain for each of the pixels reported by Hamamatsu was not reproduced since neither the level of laser light nor the laser beam were matched to the Hamamatsu irradiation conditions. The average relative difference between the two gain studies pixel-to-pixel was about 10%. As previously

discussed, the absolute gain values are a strong function of the normalization algorithm, making quantitative comparisons difficult. Nevertheless, the response of the MaPMT to the Hamamatsu irradiation and the response of the SoNDe-module prototype to the laser irradiation bore qualitative similarities. The differences in the responses likely arise from the fact that the Hamamatsu gains were determined using a uniform irradiation over the entire pixel while the laser apparatus only irradiated a relatively small central region of the pixel. The response of the SoNDe-module prototype to a central scan of a collimated alpha-particle beam with an energy of ~ 3.5 MeV was also determined. In general, the relative amount of scintillation light which was produced by the alpha particles was more than the amount of light provided by the red-laser irradiation. The pixel-to-pixel gain variations in the alpha-particle response were corrected using both the measured laser-irradiation gain matrix and the Hamamatsu data-sheet values. Qualitative similarities between the two corrected alpha particle gain maps clearly exist. Unfortunately, the data suggest a misalignment of either the collimator, the SoNDe-module prototype, or both. Leakage of scintillation light into adjacent pixels of about 20% was observed.

Worryingly, one of the pixels in the SoNDe-module prototype is already showing signs of failure.

4.2 Suggestions for improvements

In all of the laser measurements the red laser was used. In retrospect, the blue laser should have been used instead since the wavelength of the blue laser is closer to the scintillation wavelength. The reason for using the red laser was that it was easier to get the trigger signal right for this first series of measurements. Another change that could be made is to match the laser-light better with the conditions that Hamamastu used when producing their data sheet. Both the laser-light level that was used and the size of the illuminated area could be matched better. This would have resulted in a more fair comparison between the two different calibrations. Finally, an improved alpha-particle collimator would be advantageous.

4.3 Future outlook

The results presented in this thesis together with the experience gained in obtaining them provide a clear route forward in developing a better understanding of the SoNDe-module prototype. A first step is to vary the laser-light level used in the irradiations which will enable study of the per-pixel gains as a function of light level. This can be accomplished by changing the wavelength of the laser, the tune of the laser, the strength of the attenuation provided by the NDF or a

combination of these parameters. This will in turn give a better understanding of the differences obtained with different methods of calibration. Since gain variations also seem to occur within each pixel, the step size of the laser scan should be decreased resulting in sub-pixel laser scans. Different step sizes could be used and the results compared via software averaging algorithms to investigate the response of the detector as a function of the step size of the scan. This could then also be compared to the response from the central scan.

In parallel to developing a better understanding of the response of the SoNDe-module prototype to the laser beam, the understanding of the properties of the alpha-particle beam should be improved. This can be done by constructing an adjustable collimator with variable collimator insets which will allow for different source-to-prototype distances and beam-spot sizes. Further, measurements of temperature, pressure and humidity in the lab will allow for a more precise determination of the air density and thereby facilitate a better determination of the alpha-particle beam energy. This should even be measured using a dedicated alpha-particle detector.

To develop a better understanding of which features in the overall response arise from the MaPMT and which features arise from the scintillator and how it is mounted to the MaPMT, the components of the prototype should be systematically decoupled. First, the response of the MaPMT should be studied. Then the response of the MaPMT together with the scintillator dry-fitted to it should be studied. And finally, the MaPMT together with the scintillator fitted with silicon gel should be studied. Comparing these results will enable the determination of which of the components contribute what to the overall response.

The unanticipated light-leakage or “glow” phenomenon should be studied in detail as glow may result in the location of events being falsely identified. This can be done by replacing the flat scintillator wafer with a more realistic scintillator sample etched with grooves which correspond to the $6 \times 6 \text{ mm}^2$ pixels. A grooved scintillator wafer will better constrain the scintillation light to a single MaPMT pixel. Comparing the results may allow for the separation of glow effects from pixel-to-pixel crosstalk effects.

And finally, of course, the SoNDe-module prototype should be subjected to thermal neutrons!

Appendix A

Contribution of the author

Table A.1: Summary of the contribution of the author to this project.

Week	Activity
3	Background reading
4	Background reading
5	Background reading
6	Constructing optical box
7	Constructing optical box
8	Testing optical box
9	Familiarize with equipment
10	Familiarize with equipment
11	Testing MaPMT
12	Testing MaPMT
13	Testing SoNDe module
14	Testing SoNDe module
15	Prepare measurements to take in Glasgow
16	Taking measurements at the University of Glasgow
17	Setting up ROOT and data analysis
18	Data analysis
19	Data analysis
20	Break for exams
21	Break for exams
22	Break for exams
23	Writing of thesis
24	Writing of thesis
25	Writing of thesis

Appendix B

Self reflection

For the last six months, I have had the opportunity to work with the SoNniG-group on the SoNDe project. During this time, I have been faced with many challenges but gained a lot of experience and knowledge after overcoming them. The main challenge was that for the first time during my education, I was the one who needed to take all the initiative in order to get the project to moving forward. There was no predetermined plan of what should be included and instead I got to choose that along the way. Since I basically started from scratch with characterizing the detector, I have learned all the steps that are necessary, starting from setting up experiments with the NIM modules and electronics necessary to read out and analyze the data obtained.

During my time with the project, I was given the opportunity to travel to Glasgow and perform necessary measurements there. That was an experience I will always be grateful for but one which brought some difficulties with it. The main one was not being able to perform any further measurements after the trip. This gave me a new insight into how crucial planning is during trips like this when you only have limited time at the facility. From this trip (and the entire project) I also experienced how it is to work within a project that is a collaboration between different universities, which was something completely new for me.

This project has truly ignited my interest for nuclear physics, and more specifically for detector physics and because of that, I aspire to continue to work within this field after finishing my degree.

Appendix C

Construction of a light-tight optical box

C.1 Construction

To be able to test the MaPMTs without interference from surrounding lights, a light-tight optical box had to be constructed. The base for the box is an aluminum box purchased at Biltema [33] with external measurements $1120 \times 380 \times 380$ mm³. The first step towards making it light tight was removing the handles on the sides and the lock on the front, since light could easily leak through these mount points. The entire inside of the box was painted matte black to minimize any further reflection from leaked light, see Fig. C.1.

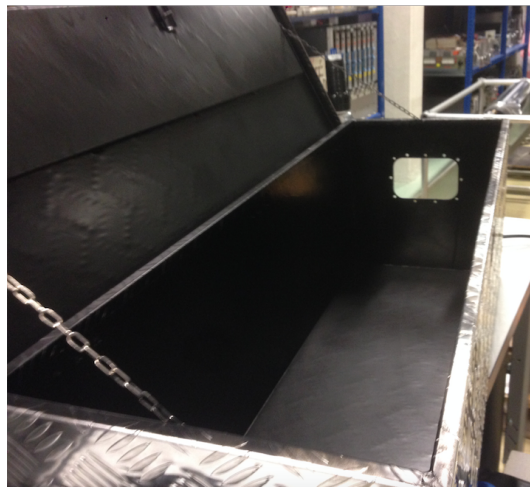


Figure C.1: First steps towards constructing the optical box. The lock and the handles have been removed since light could leak through these points. The inside was painted matte black to minimize reflections.

The next step was to construct the patch panel for the various connections which enabled signal and high voltage to be routed from the outside to the inside of the box. On the first version of the panel, two SHV high voltage connectors, four BNC connectors, and four flat band cables were attached. The edges and holes between the panel and the connectors/cables were then sealed with black silicone, see Fig. C.2.

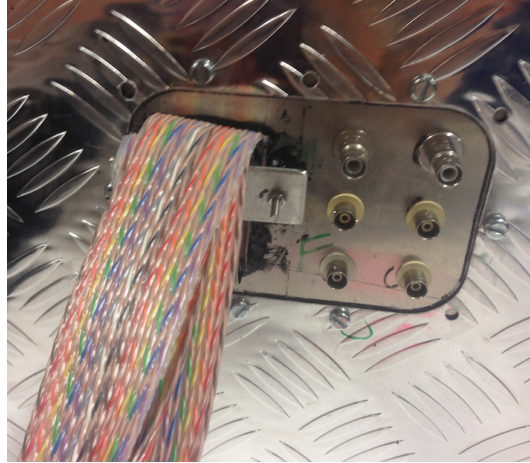


Figure C.2: First version of the patch panel. The patch panel has two SHV high voltage connectors, four BNC connectors, and four flat band cables.

The patch panel was later modified to enable the SoNDe-module to be used inside the box. One of the BNC connectors was replaced with a connector for an ethernet cable and an additional penetration was added for the power supply cable, see Fig. C.3.

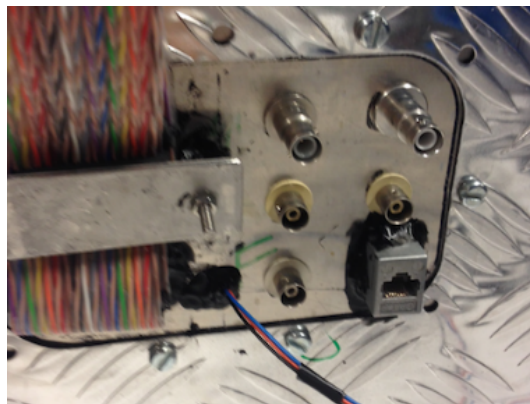


Figure C.3: Second version of the patch panel. A connector for an ethernet cable and a penetration for the power supply cable were added.

The new penetrations were sealed with black silicone to keep them light-tight. The corners and the slits were also sealed with black silicone. The last step before the box was completed was to add foam-rubber seals around the top edges where the lid met the box.

C.2 Light-tightness verification of the box

Before the box could be used, it had to be tested to see if it in fact is light tight. Initially, two smaller measurements were done using a flash light as external light source and after some improvements, a final test under typical light conditions was conducted.

C.2.1 First pre-measurement

For the first measurement, a Philips XP4312-B PMT combined with a Philips VDK 123K base was used. The applied voltage was -1700 V. The signal was read out using an oscilloscope. The setup inside the box can be seen in Fig. C.4 and the entire setup can be seen in Fig. C.5.

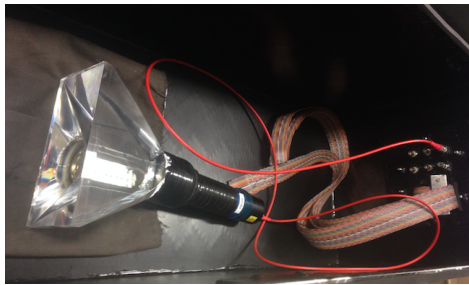


Figure C.4: Setup inside the optical box. The PMT was placed at the bottom of the box.

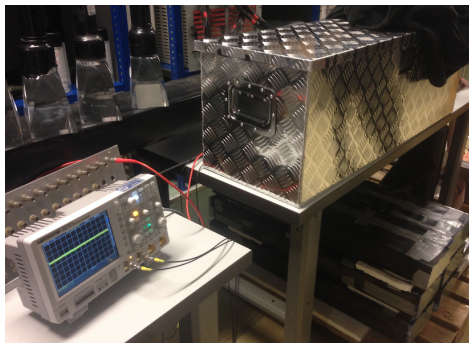


Figure C.5: Setup with the box closed.

There were three weak points found: the top front corner of the box, the connectors at the panel, and the handle on the left side of the box. When using a flash light at those areas, the signal dropped by ~ 1 mV. The weak points were strengthened.

C.2.2 Second pre-measurement

The setup for the second measurement was the same setup as for the first test. The weak spots that were discovered in the previous measurement could no longer be observed when using a flash light. The PMT was placed in three different positions in the box: left, middle and right. At each position, the PMT faced both left and right, so six measurements were taken in total. There were no noticeable differences visible on the oscilloscope after changing positions.

C.2.3 Measurement of light leakage

For the final characterization of the optical box, a Philips XP4312-B PMT combined with a Philips VDK 123K base was used. The applied voltage was -1900 V. The signal was read out on a oscilloscope and the oscilloscope had the same settings throughout the entire experiment; 5 mV/div with 2 ns/div and an auto trigger at a threshold of -3 mV DC.

Four measurements were made in different environmental settings:

1. Lights on in the room and box as dark as possible by covering with a black towel (default mode)
2. Lights on in the room and nothing extra done with the box
3. Lights off in the room and as dark as possible by covering with a black towel (optimal mode)
4. Lights off in the room and using a flash light directly onto the exterior of the box

For each run, the number of counts occurring over a 75 s period was measured and the mean pulse height of the signal which arose due to the light leaking into the box was determined. The number of counts is how many times the oscilloscope triggered which corresponds to how many signals the PMT have registered. The results are presented in Table C.1.

Table C.1: Results from the final leakage measurement of the optical box. The mean values of the recorded signals and the number of counts in 75 s for the four different measurements listed above are presented.

Setting	Mean value (10^{-4} V)	Counts in 75 s
1	1.6084 ± 0.1303	3953
2	2.5383 ± 0.2794	6946
3	1.4130 ± 0.1027	3297
4	7.1739 ± 0.6244	8186

C.3 Conclusion

It is important to emphasize that the values in Table C.1 do not mean anything on an absolute scale. They are only relevant when comparing them to each other. The mean value represents how much the measured values differ from the baseline. In the optimal case, when having no light from the surroundings and no dark current, the measured mean value is expected to be zero. This will obviously not be the case since there is always dark current and noise in the signal from the PMT. However, there is a clear difference when having light directed into the box and when not. The first three operating modes have mean values that are relatively close but there is a large difference in the number of counts for setting 1 and 3 compared to setting 2. The conclusion drawn was that setting 1 (default mode) is close enough to setting 3 (optimal mode) for the box to be considered light-tight and used.

It should also be emphasized that these measurements are only a qualitative indication of the box working for the purposes needed. This is no indication of how well it works or how much leakage occurs. For such studies, measurements have to be performed with precisely calibrated equipment. There will of course be some leakage into the box, but the amount of leaked light compared to the amount of real signal is small enough to conclude that the box is fulfilling its purpose.

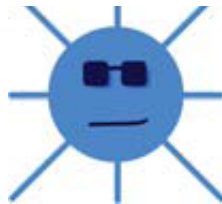
References

- [1] ESS - Technology, 2017, URL <https://europeanspallationsource.se/technology>.
- [2] James Chadwick - facts, 2014. URL http://www.nobelprize.org/nobel_prizes/physics/laureates/1935/chadwick-facts.html Accessed 2017-04-26.
- [3] K Nakamura and Group Particle Data. Review of particle physics, 2010. Journal of Physics G: Nuclear and Particle Physics, 37(7A):75021, ISSN 1674-1137. doi: 10.1088/1674-1137/38/9/090001. URL <http://stacks.iop.org/0954-3899/37/i=7A/a=075021>.
- [4] Nicholai Mauritzson. Design, construction and characterization of a portable fast-neutron detector. Master's thesis, 2017.
- [5] G.S. Bauer. Physics and technology of spallation neutron sources, 2011. Nuclear Instruments and Methods in Physics Research Section A: Accelerators, Spectrometers, Detectors and Associated Equipment, 463(3):505–543. ISSN 01689002. doi:10.1016/S0168-9002(01)00167-X. URL <http://www.sciencedirect.com/science/article/pii/S016890020100167X>.
- [6] Zohreh Gholamzadeh Seyed Amir Feghhi and Claudio Tenreiro. Investigation of the optimal material type and dimension for spallation targets using simulation methods, 2014. Journal of Theoretical and Applied Physics, 8(1):1, 2014. ISSN 2251-7235. doi: 10.1186/2251-7235-8-1. URL <http://www.jtaphys.com/content/8/1/11>.
- [7] Kenneth S. Krane. *Introductory nuclear physics*. John Wiley and Sons, 1988.
- [8] The SKADI Diffractometer: Enlarging the Field of Small-Angle Neutron Scattering, 2017, URL <https://europeanspallationsource.se/article/skadi-diffractometer-enlarging-field-small-angle-neutron-scattering>.
- [9] Hanno Perrey, Private communication, 2017.

- [10] The ESS Mandate, 2017, URL <https://europeanspallationsource.se/ess-mandate>.
- [11] D.A. Shea and D. Morgan, The helium-3 shortage: Supply, demand, and options for congress, Congressional Research Service, 2010.
- [12] Detector System for Snapshots of Biological and Chemical Processes, 2017, URL http://www.fz-juelich.de/ics/ics-1/EN/Leistungen/ESS/SonDe-Projekt/_node.html;jsessionid=5B119F3B40AC316FBE8AFA509569E308.
- [13] Laboratoire Léon-Nrillouin, 2017, URL <http://www-llb cea.fr/>.
- [14] Integrated Detector Electronics AS, 2017, URL <http://ideas.no/>.
- [15] William R. Leo. *Techniques for nuclear and particle physics experiments: a how-to approach*. Springer science and business media, 1994.
- [16] Simon M. Sze and Ming Kwei Lee. *Semiconductor Devices: Physics and Technology, 3rd Edition*. John Wiley and Sons, 2012.
- [17] Glenn F. Knoll. *Radiation detection and measurement*. John Wiley and Sons, 2010.
- [18] Scintacor, market leading 6-lithium glass bespoke to your application, 2017. URL <https://scintacor.com/products/6-lithium-glass/>.
- [19] A.R. Spowart. Neutron scintillating glasses: Part 1 activation by external charged particles and thermal neutrons, 1976. *Nuclear Instruments and Methods* 135(3):441-453. ISSN 0029-554X. doi:10.1016/0029-554X(76)90057-4. URL <http://www.sciencedirect.com/science/article/pii/0029554X76900574>.
- [20] Photomultiplier - Wikipedia, 2017, URL <https://commons.wikimedia.org/wiki/File:PhotoMultiplierTubeAndScintillator.jpg>.
- [21] T. Hakamata (Editor). Photomultiplier tubes basics and applications (third edition), 2006. URL http://www.hamamatsu.com/resources/pdf/etd/PMT_handbook_v3aE.pdf.
- [22] Hamamatsu H8500 series/H10966 series data sheet, 2011.
- [23] Emil Rofors. Fast photoneutron detection. Master's thesis, 2016.
- [24] Hamamatsu Anode Uniformity of H8500C Serial No. C9466 data sheet, 2016.
- [25] Rachel Montgomery. *A Position Sensitive Photon Detector for the CLAS 12 Ring Imaging Cerenkov Application*. PhD thesis, Glasgow University, 2013.

- [26] R.A. Montgomery. Investigation of hamamatsu h8500 phototubes as single photon detectors, 2015. Nuclear Instruments and Methods in Physics Research Section A: Accelerators, Spectrometers, Detectors and Associated Equipment 790(1):28-41. ISSN 01689002. doi:10.1016/j.nima.2015.03.068. URL <http://www.sciencedirect.com/science/article/pii/S0168900215004234>.
- [27] Advanced Laser Diode Systems A.L.S. GmbH. Picosecond injection Laser (PiLas) owner's manual. Testsheet results for PiLas system, 2004.
- [28] Thorlabs Ltd. NRT series motorised translation stage. User Guide.
- [29] Hamamatsu Board-Level Camera for OEM Solution C9260-901, -902, -904, -905 data sheet, 2005.
- [30] Y.A. Akovali. 241 am decay from 1994-98(nsr). URL <http://nucleardata.nuclear.lu.se/toi/nuclide.asp?iZA=950241>.
- [31] L. Gordan Greeniaus. *Triumf Kinematics Handbook*, year =.
- [32] B. Jamieson and L.A. Rebenitsch. Determining the 6li doped side of a glass scintillator for ultra cold neutrons, 2015. Nuclear Instruments and Methods in Physics Research Section A: Accelerators, Spectrometers, Detectors and Associated Equipment 790(1):6-9. ISSN 01689002. doi:10.1016/j.nima.2015.04.022. URL <http://www.sciencedirect.com/science/article/pii/S0168900215004957>.
- [33] Biltema aluminum toolbox, URL <http://www.biltema.se/sv/Verktyg/Arbetsbank-och-forvaring/Verktygslada/Verktygslada-aluminium-2000023545/>.

The project reported on in this thesis
was performed in collaboration with



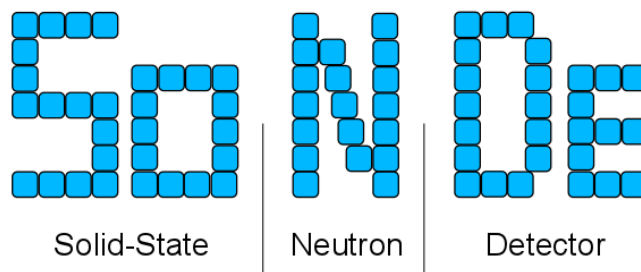
The Source-based Neutron Irradiation Group of the
Division of Nuclear Physics at Lund University

and



The Detector Group of the European Spallation Source ERIC

with support from



The Horizon 2020 Solid-state Neutron Detector (SoNDe) Project,
Proposal ID 654124